

# Calibration of imperfect mathematical models by multiple sources of data with measurement bias

Mengyang Gu\* and Kyle Anderson\*\*

\* Department of Applied Mathematics and Statistics, Johns Hopkins University  
\*\* Volcano Science Center, U.S. Geological Survey

## Abstract

Model calibration involves using experimental or field data to estimate the unknown parameters of a mathematical model. This task is complicated by discrepancy between the model and reality, and by possible bias in the data. We consider model calibration in the presence of both model discrepancy and measurement bias using multiple sources of data. Model discrepancy is often estimated using a Gaussian stochastic process (GaSP), but it has been observed in many studies that the calibrated mathematical model can be far from the reality. Here we show that modeling the discrepancy function via a GaSP often leads to an inconsistent estimation of the calibration parameters even if one has an infinite number of repeated experiments and infinite number of observations in a fixed input domain in each experiment. We introduce the scaled Gaussian stochastic process (S-GaSP) to model the discrepancy function. Unlike the GaSP, the S-GaSP utilizes a non-increasing scaling function which assigns more probability mass on the smaller  $L_2$  loss between the mathematical model and reality, preventing the calibrated mathematical model from deviating too much from reality.

We apply our technique to the calibration of a geophysical model of Kīlauea Volcano, Hawai‘i, using multiple radar satellite interferograms. We compare the use of models calibrated using multiple data sets simultaneously with results obtained using stacks (averages). We derive distributions for the maximum likelihood estimator and Bayesian inference, both implemented in the “RobustCalibration” package available on CRAN. Analysis of both simulated and real data confirm that our approach can identify the measurement bias and model discrepancy using multiple sources of data, and provide better estimates of model parameters.

KEYWORDS: aggregated data, ground deformation, InSAR, Kīlauea Volcano, model discrepancy, scaled Gaussian stochastic process

# 1 Introduction

The advancement of science has given rise to the description of various phenomena in physics, chemistry, biology and engineering as sets of generally agreed upon systems of equations or mathematical models. One typically wishes to estimate the unobserved parameters in a mathematical model using experimental observations or field data – a process generally known as model calibration (or data inversion). Estimated model parameters are usually of direct scientific interest, and properly calibrated models are also necessary if one wishes to predict reality at unobserved points.

As the mathematical model is almost always an imperfect representation of reality, much recent work on model calibration has focused on inclusion of a (usually statistical) discrepancy function. In [28], the discrepancy function is modeled as a Gaussian stochastic process (GaSP), and in combination with the calibrated mathematical model often leads to more precise predictions of reality. However, various studies have found that calibration parameters and the discrepancy function cannot be uniquely estimated. This “identifiability issue” degrades model parameter estimates and the ability of the calibrated mathematical model to predict reality [50, 53].

Model calibration is also complicated by spatially correlated patterns of measurement error, caused by the device or field conditions, which we term *measurement bias*. It is important to clarify the difference between the model discrepancy and measurement bias. The model discrepancy explains the difference between the mathematical model and physical reality and is shared in all data sources, while the measurements bias may change between different data sources. Separating the measurement bias from model discrepancy is important, for instance, as it may give insight into methods for improving the precision of the measurements. In this work we will explain these concepts in more detail using both mathematics and real examples.

Even though measurement biases are reported in many previous studies [14, 26, 55], the simultaneous analysis of both measurement bias and model discrepancy has rarely been considered. Both effects were considered in [40], but the model discrepancy in that work is defined as a linear trend of the predictors, which might not be suitable in other studies. In this work, we introduce a statistical method utilizing multiple sources of data to address the uncertainty of the calibration parameters, model discrepancy, measurement bias, and noise. The GaSP model of the discrepancy function has been found to be confounded with parameters of the mathematical models when using one source of data without measurement bias [6, 50, 53]. The scaled Gaussian stochastic process (S-GaSP) was introduced in [20, 22] to better address the identifiability problem between the mathematical model and reality. We study both methods when multiple sources of data are available, and will argue that the S-GaSP offers advantages in modeling the discrepancy function separating the measurement bias and model discrepancy, which has not been studied before.

We apply our technique to the scientific problem of using satellite interferograms to calibrate a geophysical model of Kīlauea Volcano. However, we emphasize that the methods developed in this work are general for a wide range of problems in model calibration and data fusion.

## 1.1 InSAR and volcano deformation

The Earth’s surface is deformed on a wide range of spatial and temporal scales by processes such as earthquakes, volcanic eruptions, and withdrawal of subsurface fluids such as hydrocarbons and groundwater. Measurements of this deformation are important for hazard monitoring and for

constraining source processes. Over the last 25 years, satellite-based radar measurements have made it possible to map deformation over broad swathes of the Earth’s surface to sub-centimeter accuracy from space, revolutionizing scientists’ ability to record and model deformation of the Earth’s surface due to processes such as earthquakes and volcanic eruptions [34, 35].

Interferometric synthetic aperture radar (InSAR) images (interferograms) are most often obtained using data from orbiting microwave-band radar satellites. By ‘interfering’ two radar images of the surface taken from a satellite at approximately the same location but at different times, changes in radar phase are obtained which record temporal changes in the position of the Earth’s surface along the oblique line-of-sight (LoS) vector between satellite and ground. Because only fractional phase change can be measured directly (the number of complete phase cycles between the satellite and ground is not known), these images are wrapped by the radar’s wavelength. “Unwrapping” an image by spatial integration of the phase gradient – relative to a point believed to be non-deforming – yields relative LoS deformation, in units of distance change [11]. It is these unwrapped images which are most commonly modeled.

InSAR observations have been reported for hundreds of Earth’s volcanoes [9]. Because volcano deformation is typically ascribed to the motion of magma or magmatic fluids in the subsurface, these data have revolutionized scientists’ ability to observe and model magmatic processes at the world’s volcanoes [1, 10, 32, 41, 52]. As latency times have decreased, InSAR observations have also become increasingly useful for hazard monitoring and response during ongoing volcanic crises.

Despite these advances, the interpretation of InSAR data is often greatly complicated by atmospheric noise which contaminates many images, as well as assumptions and simplifications in the geophysical source models used in InSAR data interpretation.

## 1.2 Noise and measurement bias in InSAR data

Noise in InSAR data – introduced by the radar system, by the atmosphere, by reflectors (scatterers) on the ground, and in processing [10] – obscures our ability to resolve surface deformation and can bias source estimates. After removing phase due to the elevation of the Earth’s surface, the wrapped phase  $\phi$  for each pixel on the ground may be described by (e.g., [26])

$$\phi = W \{ \phi_d + \phi_a + \phi_o + \phi_l + \phi_n \}, \quad (1)$$

where  $W$  is a “wrapping” operator that drops full phase cycles,  $\phi_d$  is due to LoS ground displacement,  $\phi_a$  is propagation delay due to the atmosphere (tropospheric water vapor and ionospheric electron density [16]),  $\phi_o$  is residual phase due to satellite orbital errors,  $\phi_l$  is residual phase due to look angle error, and  $\phi_n$  is a noise term accounting for remaining noise (scattering variability, thermal noise, etc.) [26]. Note that the unwrapping procedure removes the  $W$  operator to convert phase  $\phi$  to actual ground displacements, which is typically modeled.

Of the sources of uncertainty in equation (1), the spatially-correlated atmospheric term  $\phi_a$  is the most important; spatial and temporal changes of just 20% in relative humidity lead to errors of 10 cm in estimated ground deformation [55]. These errors exhibit strong spatial correlations. Figure 1b shows wrapped InSAR phase at Kīlauea Volcano (section 1.3). A “bullseye” pattern near the center of the image is due to real ground deformation  $\phi_d$ , while most of the remaining fringes are due to  $\phi_a$ . Atmospheric signal may be directly estimated and removed with weather models or the data from continuous GPS or optical satellites (e.g., [13]), or if enough data are available

reduced through sophisticated time series analyses [25], but these approaches cannot always be applied and only imperfectly remove atmospheric noise, and remaining errors often reduce effective accuracy from several millimeters to several centimeters [16]. In this work, measurement bias – mainly caused by atmospheric errors – is incorporated into a coherent statistical model of the InSAR data.

Covariance matrices for InSAR data are typically estimated by empirical autocovariance using a selection of points in regions believed to be non-deforming, under the stationary and isotropic assumptions [31]. However, this approach can introduce bias, for instance if noise in the non-deforming region is different than that in the deforming region. In this work, the measurement bias in each InSAR interferogram is modeled by a Gaussian stochastic process with an anisotropic Matérn covariance function, together with the geophysical model and discrepancy function, in a coherent statistical model. The use of anisotropic Matérn covariance was previously suggested in [29] to improve the precision in estimating InSAR data covariance (and model parameter estimates) and as being consistent with tropospheric delay models, but this approach has not been commonly employed.

Stacking (averaging) multiple interferograms is often used to reduce noise and bias which varies between images, and also reduces the number of observations which must be modeled [47, 55]. In this work, we show that under certain assumptions, some usual estimators, such as the maximum likelihood estimator of the calibration parameters inferred from a stacked image, are equivalent to those estimated from simultaneous consideration of all images. This does not hold true, however, if the different measurement biases appear in the images, as may occur due to correlation of atmospheric artifacts with Earth topography. In this work, the approach of separating atmospheric artifacts and model discrepancy using individual satellite images will be compared to the results obtained by image stacking. When the number of images is large, we establish the connection between the limiting distribution of the models of the stacked image with and without the measurement bias.

### 1.3 Modeling volcanic unrest with InSAR data: Kīlauea Volcano

Kīlauea Volcano, on the Island of Hawai‘i, is one of the world’s most active volcanoes and erupted almost continuously from 1983 to 2018. InSAR data have been widely used at Kīlauea to estimate the locations and volume changes of reservoirs and magma intrusions [7, 33, 37, 42], to resolve flank stability [12], and – together with other data sets – to resolve magma supply rate and the concentration of volatiles in Kīlauea’s primary (source) magma [3, 4].

Figure 1 shows InSAR ground displacement at Kīlauea from October, 2011 to May, 2012, when the summit of Kīlauea inflated due to magma storage [3]. These data were recorded from a satellite orbiting roughly north to south (“descending mode”), and recording LoS deformation (‘looking’) along a vector oblique to the Earth’s surface – roughly east to west and downwards at an angle of 41 degrees. This image thus resolves a combination of predominantly vertical and east-west ground deformation. To best constrain 3D ground deformation patterns it is therefore desirable to utilize data from satellites with different look vectors. Finally, the image was subsampled using the quadtree algorithm (Figure 1d) which is widely used to reduce the number of pixels in the InSAR interferogram [27].

InSAR data from volcanoes are most commonly interpreted using analytical elastic halfspace models which are derived from the principals of continuum mechanics [e.g. 36, 54]. These models

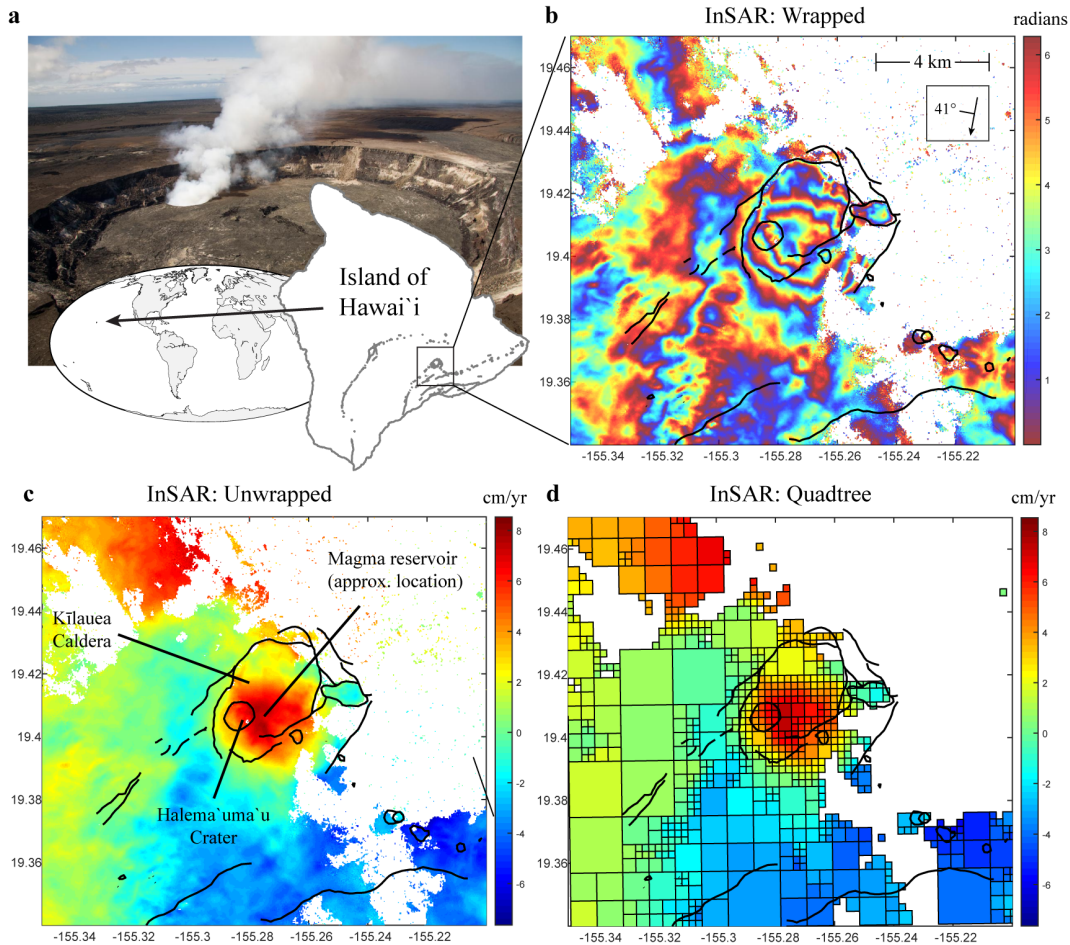


Figure 1: a) Overview maps showing the location of Kilauea Volcano on the Island of Hawai'i, with background photo of Halema'uma'u Crater at the volcano's summit roughly as it appeared during the time of this study (USGS photo). (b) Wrapped InSAR interferogram from the COSMO-SkyMed satellite, spanning 20 Oct 2011 to 15 May 2012. The inset box shows the flight path of the satellite (arrow) and the downward look direction of the satellite at  $41^\circ$ . White areas have no data due to radar decorrelation. Number of data points is approximately  $1.5 \times 10^5$  (note that full uncropped interferograms span a much broader geographical region and have many more pixels). (c) Same data as in (b), but unwrapped. (d) Quadtree-processed interferogram, with 705 data points, a reduction of roughly  $200\times$ . Thick black lines in panels b-d show cliffs and other important topographic features at the volcano; the large elliptical feature is Kilauea Caldera. Thin black lines in panel d show edges of the quadtree boxes. Data are from [3].

relate volume and pressure changes in buried cavities of various shapes to surface displacements. Given observed ground deformation data, our goal is to resolve the location (and possibly shape) of the magma reservoir, and the change in volume of the reservoir cavity during the time period of our observations.

We relate ground displacements to properties of the magma reservoir using a geophysical model of an inflating magma reservoir in an elastic crust. We denote the geophysical model by  $f^M(\mathbf{x}, \boldsymbol{\theta})$ , where  $\mathbf{x}$  are observable and  $\boldsymbol{\theta}$  are unobservable. We choose a simple model [36] for which a closed-

form analytical solution is available. This model is widely used and has been shown capable of broadly reproducing ground deformation observed at many volcanoes, to first order. For [36] the model parameter vector is given by  $\boldsymbol{\theta} = (\theta_1, \theta_2, \theta_3, \theta_4, \theta_5)^T$ , where  $\theta_1$ ,  $\theta_2$ , and  $\theta_3$  are the 3D coordinates of the reservoir centroid within the earth,  $\theta_4$  is the rate of reservoir volume change, and  $\theta_5$  is a material property (Poisson’s ratio) which over a plausible apriori range does not strongly affect the outcome of the geophysical model and is typically considered a nuisance parameter. 3D ground displacements predicted by the model are converted to 1D LoS displacements by taking the dot product of the 3D deformation vector at each point on the ground with the unit vector describing the LoS. Because we assume that the look vectors are perfectly known, they do not appear in  $\boldsymbol{\theta}$ . Note that we utilize observations from more than one look angle, and this process must be repeated for each interferogram.

We highlight several primary challenges in calibrating the mathematical model. First, the class of geophysical models considered herein assumes a very simple earth structure and a spherical source geometry, which might not be able to explain all the variability in the reality. Secondly, the interferograms may be affected by atmospheric conditions and other sources of error (e.g. the northwest region in Figure 1c is atmospheric noise). Interferograms also yield a relative measure of ground deformation, from which absolute deformation must be inferred relative to a point assumed to be non-deforming. Since this point is not known precisely, an uncertain mean value shift is contained in each interferogram. And, finally, the number of pixels in InSAR images can be very large and can become computationally prohibitive in a calibration (inverse) problem.

These issues are addressed as follows in this paper. In Section 2, we introduce a new statistical model that includes both the discrepancy function and measurement bias using multiple sources of field data. The marginal likelihood and the predictive distribution of the new model are derived for the estimation of the calibration parameters, reality, model discrepancy and measurement bias. Section 3 discusses the statistical model of the discrepancy function and measurement bias. The parameter estimation via the full Bayesian inference is discussed in Section 4. The simulated and real numerical evidence comparing several models are given in Section 5 and a short conclusion is given in Section 6. Proofs of lemmas and theorems are provided in the Appendix.

## 2 Model calibration by multiple sources of data

In this section, we introduce a statistical framework that addresses the uncertainty in imperfect mathematical models and observations from multiple sources in Section 2.1. The connection and difference between modeling the full data and aggregated data is discussed in Section 2.2.

### 2.1 A framework of modeling multiple imperfect measurements

Denote  $y_l^F(\mathbf{x})$  the real-valued field data at the observable variable input  $\mathbf{x} \in \mathcal{X}$  from the source  $l$ ,  $l = 1, \dots, k$ . The mathematical model is defined as  $f^M(\mathbf{x}, \boldsymbol{\theta})$ , where  $\boldsymbol{\theta}$  denotes the unobservable calibration parameters. As  $y_l^F(\mathbf{x})$  and  $f^M(\mathbf{x}, \boldsymbol{\theta})$  may be both imperfect, we consider the model

$$\mathbf{y}_l^F(\mathbf{x}) = f^M(\mathbf{x}, \boldsymbol{\theta}) + \delta(\mathbf{x}) + \delta_l(\mathbf{x}) + \mu_l + \epsilon_l, \quad (2)$$

where  $\mu_l$  is a mean parameter of the source  $l$  and  $\epsilon_l \sim N(0, \sigma_{0l}^2)$  is an independent Gaussian noise with variance  $\sigma_{0l}^2$ , for each  $\mathbf{x}$  and for source  $l = 1, \dots, k$ . In model (2),  $\delta(\cdot)$  and  $\delta_j(\cdot)$  denote

the model discrepancy function and the  $l$ th measurement bias function, respectively. For any inputs  $\{\mathbf{x}_1, \dots, \mathbf{x}_n\}$ , we assume that the marginal distributions of  $\boldsymbol{\delta} := (\delta(\mathbf{x}_1), \dots, \delta(\mathbf{x}_n))^T$  and  $\boldsymbol{\delta}_l := (\delta_l(\mathbf{x}_1), \dots, \delta_l(\mathbf{x}_n))^T$  both independently follow zero-mean multivariate normal distributions

$$\boldsymbol{\delta} \sim \text{MN}(\mathbf{0}, \tau^2 \mathbf{R}), \quad (3)$$

$$\boldsymbol{\delta}_l \sim \text{MN}(\mathbf{0}, \sigma_l^2 \mathbf{R}_l), \quad (4)$$

where  $\tau^2 \mathbf{R}$  and  $\sigma_l^2 \mathbf{R}_l$  are the covariance matrices, with  $\tau^2$  and  $\sigma_l^2$ , being the variance parameters for  $l = 1, \dots, k$ , respectively. The  $(i, j)$ th term of  $\mathbf{R}$  and  $\mathbf{R}_l$  are often parameterized by the kernel functions  $K(\mathbf{x}_i, \mathbf{x}_j)$  and  $K_l(\mathbf{x}_i, \mathbf{x}_j)$ ,  $l = 1, \dots, k$ , and  $1 \leq i, j \leq n$ . We postpone the discussion of kernel functions to Section 3.

In model (2), the physical reality, denoted as  $y^R(\mathbf{x})$  at any coordinate  $\mathbf{x}$ , can be expressed as the summation of the mathematical model and discrepancy function, i.e.  $y^R(\mathbf{x}) = f^M(\mathbf{x}, \boldsymbol{\theta}) + \delta(\mathbf{x})$ , which follows the construction introduced in [28]. The innovation of the model (2) is to explicitly model the measurement bias contained in the observations.

For our scientific goal, long-wavelength ‘‘ramp’’ artifacts may appear in InSAR data due to errors in satellite orbits. Linear or quadratic ramp parameters may be estimated together with geophysical model parameters if the ramps cannot be corrected independently (for instance using data from GPS sensors) [47]. Here for simplicity, and because the area of geographic area of interest is relatively small, we assume that linear and higher-order ramp terms are negligible. Because InSAR measures ground displacements relative to a subjective point assumed to be non-deforming, however, we must account for possible error in the mean value of each image. Hence, we assume an unknown mean parameter  $\mu_l$  for the  $l$ th interferogram, where  $l = 1, \dots, k$ , in model (2). In general, the intercept and trend in the observations can be modeled as a mean function  $\mu_l(\cdot)$  in model (2), if they are not captured in the mathematical model.

The assumption in (2) that measurement bias terms are independent may be violated in practice. To reduce dependency between the sources (InSAR images), we only use interferograms which do not share any acquisition times. When the measurement bias is not independent, one may model the data from different sources in a latent factor model, where the factor loading matrix is often estimated by the correlation between each source of the data. However, estimating the correlation between each source of the data introduces extra dimensions of difficulties in calibration, and thus we do not pursue this direction in this work. A possible approach to model the dependency across sources is through the linear model of coregionalization (LMC) [15]. The principal component analysis was used to estimate the loading matrix in LMC in calibration [23], and a new way of estimating the loading matrix was recently introduced in [19].

The observations from the  $l$ th source of data are denoted as  $\mathbf{y}_l^F = (y_l^F(\mathbf{x}_1), \dots, y_l^F(\mathbf{x}_n))^T$  at  $\{\mathbf{x}_1, \dots, \mathbf{x}_n\}$ , for  $l = 1, \dots, k$ . For the InSAR interferograms, each entry of  $\mathbf{y}_l^F$  represents a line-of-sight displacement at a point on the Earth’s surface. The following lemma gives the marginal distribution of model (2), after integrating out the random measurement bias functions.

**Lemma 1.** *After integrating out  $\boldsymbol{\delta}_l$  in model (2),  $l = 1, \dots, k$ , one has the following distributions:*

1. *For each source  $l = 1, \dots, k$ , the marginal distribution of the field data follows a multivariate normal distribution*

$$(\mathbf{y}_l^F \mid \boldsymbol{\delta}, \boldsymbol{\theta}, \sigma_l^2, \mathbf{R}_l, \mu_l, \sigma_{0l}^2) \sim \text{MN}(\mathbf{f}_\theta^M + \mu_l \mathbf{1}_n + \boldsymbol{\delta}, \sigma_l^2 \mathbf{R}_l + \sigma_{0l}^2 \mathbf{I}_n), \quad (5)$$

where  $\mathbf{f}_\theta^M = (f^M(\mathbf{x}_1, \theta), \dots, f^M(\mathbf{x}_n, \theta))^T$  and  $\boldsymbol{\delta} = (\delta(\mathbf{x}_1), \dots, \delta(\mathbf{x}_n))^T$ , with  $\mathbf{I}_n$  being an  $n \times n$  identity matrix.

2. The marginal posterior distribution of the discrepancy function follows a multivariate normal distribution

$$(\boldsymbol{\delta} \mid \{y_l^F, \sigma_l^2, \mathbf{R}_l, \sigma_{0l}^2, \mu_l\}_{l=1}^k, \boldsymbol{\theta}, \tau^2, \mathbf{R}) \sim \text{MN}(\hat{\boldsymbol{\delta}}, \hat{\boldsymbol{\Sigma}}), \quad (6)$$

where

$$\hat{\boldsymbol{\Sigma}} = \left( \sum_{l=1}^k \tilde{\boldsymbol{\Sigma}}_l^{-1} + (\tau^2 \mathbf{R})^{-1} \right)^{-1} \quad \text{and} \quad \hat{\boldsymbol{\delta}} = \hat{\boldsymbol{\Sigma}} \sum_{l=1}^k \tilde{\boldsymbol{\Sigma}}_l^{-1} \tilde{\mathbf{y}}_l,$$

with

$$\tilde{\mathbf{y}}_l = \mathbf{y}_l - \mathbf{f}_\theta^M - \mu_l \mathbf{1}_n \quad \text{and} \quad \tilde{\boldsymbol{\Sigma}}_l = \sigma_l^2 \mathbf{R}_l + \sigma_{0l}^2 \mathbf{I}_n.$$

Further marginalizing out  $\boldsymbol{\delta}$ , the marginal distribution of the field data  $\mathbf{Y}_v^F := ((\mathbf{y}_1^F)^T, \dots, (\mathbf{y}_k^F)^T)^T$  is given in the following lemma.

**Lemma 2.** *After integrating out both  $\boldsymbol{\delta}$  and  $\boldsymbol{\delta}_l$ ,  $l = 1, \dots, k$ , the marginal distribution of the field data follows a multivariate normal distribution*

$$(\mathbf{Y}_v^F \mid \{\sigma_l^2, \mathbf{R}_l, \sigma_{0l}^2, \mu_l\}_{l=1}^k, \boldsymbol{\theta}, \tau^2, \mathbf{R}) \sim \text{MN}(\mathbf{1}_k \otimes \mathbf{f}_\theta^M + \boldsymbol{\mu} \otimes \mathbf{1}_n^T, \tau^2 \mathbf{1}_k \mathbf{1}_k^T \otimes \mathbf{R} + \boldsymbol{\Lambda}), \quad (7)$$

where  $\otimes$  denotes the Kronecker product,  $\boldsymbol{\mu} = (\mu_1, \dots, \mu_k)^T$  and  $\boldsymbol{\Lambda}$  is a  $kn \times kn$  block diagonal matrix, with the  $l$ th diagonal block being  $\tilde{\boldsymbol{\Sigma}}_l$  defined in Lemma 1,  $l = 1, \dots, k$ . The density of (7) can be expressed as

$$\begin{aligned} p(\mathbf{Y}_v^F \mid \{\sigma_l^2, \mathbf{R}_l, \sigma_{0l}^2, \mu_l\}_{l=1}^k, \boldsymbol{\theta}, \tau^2, \mathbf{R}) \\ = (2\pi)^{-\frac{nk}{2}} \tau^{-n} |\mathbf{R}|^{-\frac{1}{2}} |\hat{\boldsymbol{\Sigma}}|^{\frac{1}{2}} \prod_{l=1}^k |\tilde{\boldsymbol{\Sigma}}_l|^{-\frac{1}{2}} \exp \left\{ -\frac{1}{2} \left( \sum_{l=1}^k \tilde{\mathbf{y}}_l^T \tilde{\boldsymbol{\Sigma}}_l^{-1} \tilde{\mathbf{y}}_l - \left( \sum_{l=1}^k \tilde{\boldsymbol{\Sigma}}_l^{-1} \tilde{\mathbf{y}}_l \right)^T \hat{\boldsymbol{\Sigma}}^{-1} \left( \sum_{l=1}^k \tilde{\boldsymbol{\Sigma}}_l^{-1} \tilde{\mathbf{y}}_l \right) \right) \right\}, \end{aligned}$$

where  $\hat{\boldsymbol{\Sigma}}$ ,  $\tilde{\mathbf{y}}_l$ , and  $\tilde{\boldsymbol{\Sigma}}_l$  are defined in Lemma 1, for  $l = 1, \dots, k$ .

Both Lemma 1 and Lemma 2 can be used for computing the likelihood given the other parameters in the full Bayesian analysis. Lemma 2 may be used to develop the maximum likelihood estimator, as both the random model discrepancy and measurement bias functions are marginalized out explicitly. Note that the computational complexity of the marginal density of the field data is  $O((k+1)n^3)$  in both lemmas, for inverting  $k+1$  covariance matrices, each with the size  $n \times n$ , rather than  $O((kn)^3)$ , even if the covariance matrix in (7) is  $nk \times nk$  in Lemma 2. Such simplification is the key to proceed without approximations to compute the likelihood, if  $n$  is not very large. Note that the simplifications of computation rely on the aligned measurements of each source of field data. When the measurements are misaligned, approximations might be needed when the number of sources is large.

Since the discrepancy function between the mathematical model and reality is often scientifically important, one can draw and record  $\delta$  using Lemma 1 in the posterior sampling. The following theorem gives the predictive distribution at any input  $\mathbf{x}$ , given the parameters and posterior samples of  $\boldsymbol{\delta}$ .

**Theorem 1.** For any  $\mathbf{x}^* \in \mathcal{X}$ , one has the following predictive distributions for model (2):

1. The predictive distribution of model discrepancy at any input  $\mathbf{x}^*$  follows a normal distribution

$$(\delta(\mathbf{x}^*) \mid \boldsymbol{\delta}, \{\mathbf{y}_l^F, \sigma_l^2, K_l(\cdot, \cdot), \sigma_{0l}^2, \mu_l\}_{l=1}^k, \boldsymbol{\theta}, \tau^2, K(\cdot, \cdot)) \sim \mathcal{N}(\hat{\delta}(\mathbf{x}^*), \tau^2 \hat{K}^{**}),$$

where  $\hat{\delta}(\mathbf{x}^*) = \mathbf{r}(\mathbf{x}^*)^T \mathbf{R}^{-1} \boldsymbol{\delta}$ ,  $\mathbf{r}(\mathbf{x}^*) = (K(\mathbf{x}^*, \mathbf{x}_1), \dots, K(\mathbf{x}^*, \mathbf{x}_n))^T$ , and  $\hat{K}^{**} = K(\mathbf{x}^*, \mathbf{x}^*) - \mathbf{r}(\mathbf{x}^*)^T \mathbf{R}^{-1} \mathbf{r}(\mathbf{x}^*)$ .

2. For each source  $l$ ,  $l = 1, \dots, k$ , the predictive distribution of the measurement bias at any input  $\mathbf{x}^*$  follows a normal distribution

$$(\delta_l(\mathbf{x}^*) \mid \boldsymbol{\delta}, \{\mathbf{y}_l^F, \sigma_l^2, K_l(\cdot, \cdot), \sigma_{0l}^2, \mu_l\}_{l=1}^k, \boldsymbol{\theta}, \tau^2, K(\cdot, \cdot)) \sim \mathcal{N}(\hat{\delta}_l(\mathbf{x}^*), \sigma_l^2 \hat{K}_l^{**}),$$

where  $\hat{\delta}_l(\mathbf{x}^*) = \sigma_l^2 \mathbf{r}_l(\mathbf{x}^*)^T \tilde{\boldsymbol{\Sigma}}_l^{-1} (\tilde{\mathbf{y}}_l^F - \boldsymbol{\delta})$  and  $\hat{K}_l^{**} = K_l(\mathbf{x}^*, \mathbf{x}^*) - \sigma_l^2 \mathbf{r}_l(\mathbf{x}^*)^T \tilde{\boldsymbol{\Sigma}}_l^{-1} \mathbf{r}_l(\mathbf{x}^*)$ , with  $\mathbf{r}_l(\mathbf{x}^*) = (K_l(\mathbf{x}^*, \mathbf{x}_1), \dots, K_l(\mathbf{x}^*, \mathbf{x}_n))^T$ ,  $\tilde{\mathbf{y}}_l^F$  and  $\tilde{\boldsymbol{\Sigma}}_l^{-1}$  being defined in Lemma 1, for  $l = 1, \dots, k$ .

3. For each source  $l$ ,  $l = 1, \dots, k$ , the predictive distribution of the field data at any input  $\mathbf{x}^*$  follows a normal distribution

$$(y_l^F(\mathbf{x}^*) \mid \boldsymbol{\delta}, \{\mathbf{y}_l^F, \sigma_l^2, K_l(\cdot, \cdot), \sigma_{0l}^2, \mu_l\}_{l=1}^k, \boldsymbol{\theta}, \tau^2, K(\cdot, \cdot)) \sim \mathcal{N}(\hat{y}_l^F(\mathbf{x}^*), \tau^2 \hat{K}^{**} + \sigma_l^2 \hat{K}_l^{**} + \sigma_{0l}^2),$$

where  $\hat{y}_l^F(\mathbf{x}^*) = \hat{\delta}(\mathbf{x}^*) + \hat{\delta}_l(\mathbf{x}^*) + f^M(\mathbf{x}^*, \boldsymbol{\theta}) + \mu_l$ .

Lemma 1 and Theorem 1 above will be used in the full Bayesian analysis discussed in Section 4. Model (2) provides a general statistical framework that addresses the uncertainty in both model discrepancy and measurement bias using multiple sources of field data. Although the computational cost scales linearly with the number of data sources, it may still become prohibitive with many sources, and in some applications only aggregated data may be available. In geoscience, the stack image of the satellite interferograms is frequently used to reduce the computational operations. The difference of modeling the full data and aggregated data, such as the stack image, is discussed in Section 2.2.

## 2.2 Model calibration by aggregated data

Consider a special case of model (2), where each interferogram has no measurement bias, and the mean parameter and measurement noise variance are shared between all sources of the field data:

$$y_l^F(\mathbf{x}) = f^M(\mathbf{x}, \boldsymbol{\theta}) + \delta(\mathbf{x}) + \mu + \epsilon_l, \quad (8)$$

where  $\epsilon_l \sim \mathcal{N}(0, \sigma_0^2)$  is an independent Gaussian noise, for each  $\mathbf{x}$  and for  $l = 1, \dots, k$ . Assume  $\delta(\cdot)$  is the random discrepancy function such that the marginal distribution follows equation (3). Model (8) was previously used in calibration using repeated experimental data [8].

Denote  $\bar{y}^F(\mathbf{x}) = \sum_{l=1}^k y_l^F(\mathbf{x})/k$  the average value of the field data at the input  $\mathbf{x}$ . When (8) is assumed, it implies the model of the aggregated data

$$\bar{y}^F(\mathbf{x}) = f^M(\mathbf{x}, \boldsymbol{\theta}) + \delta(\mathbf{x}) + \mu + \bar{\epsilon}, \quad (9)$$

where  $\bar{\epsilon} \sim N(0, \sigma_0^2/k)$  independently for each  $\mathbf{x}$ .

Denote  $\mathbf{y}_l^F = (y_l^F(\mathbf{x}_1), \dots, y_l^F(\mathbf{x}_n))^T$  the observations in the source  $l$ ,  $l = 1, \dots, k$ , and denote  $\bar{\mathbf{y}}^F = (\sum_{l=1}^k y_l^F(\mathbf{x}_1)/k, \dots, \sum_{l=1}^k y_l^F(\mathbf{x}_n)/k)^T$  the aggregated data. Although  $\bar{\mathbf{y}}^F$  is often used for analyzing geophysical models, the relation between modeling the stack image in (9) versus modeling the full data in (8) is not generally known. The lemma below connects these approaches.

**Lemma 3.** *Denote  $\ell(\boldsymbol{\theta}, \boldsymbol{\delta}, \mu, \sigma_0^2)$  and  $\bar{\ell}(\boldsymbol{\theta}, \boldsymbol{\delta}, \mu, \sigma_0^2)$  the natural logarithm of the likelihood in model (8) and model (9). One has*

$$\ell(\boldsymbol{\theta}, \boldsymbol{\delta}, \mu, \sigma_0^2) = c(\sigma_0^2) + \bar{\ell}(\boldsymbol{\theta}, \boldsymbol{\delta}, \mu, \sigma_0^2), \quad (10)$$

where

$$\bar{\ell}(\boldsymbol{\theta}, \boldsymbol{\delta}, \mu, \sigma_0^2) = -\frac{n}{2} \log\left(\frac{2\pi\sigma_0^2}{k}\right) - \frac{kS^2(\boldsymbol{\theta}, \boldsymbol{\delta}, \mu)}{2\sigma_0^2},$$

with  $S^2(\boldsymbol{\theta}, \boldsymbol{\delta}, \mu) = (\bar{\mathbf{y}}^F - \boldsymbol{\delta} - \mu\mathbf{1}_n)^T (\bar{\mathbf{y}}^F - \boldsymbol{\delta} - \mu\mathbf{1}_n)$  and  $c(\sigma_0^2) = -\frac{n(k-1)}{2} \log(2\pi\sigma_0^2) - \frac{n}{2} \log(k) - \sum_{l=1}^k \frac{(\mathbf{y}_l^F - \bar{\mathbf{y}}^F)^T (\mathbf{y}_l^F - \bar{\mathbf{y}}^F)}{2\sigma_0^2}$ .

Lemma 3 is a direct consequence of density of the models in (8) and in (9). The result in Lemma 3 is important, as it implies some frequently used estimators, such as the maximum likelihood estimator (MLE) for  $\boldsymbol{\theta}$  and  $\mu$  after integrating out  $\boldsymbol{\delta}$ , are exactly the same using the model of the aggregated data in (9) or the model of the full data in (8). This validates the use of stack image in calibration for estimating the calibration parameters and mean parameter if model (8) is appropriate.

When  $\sigma_0^2$  is known, the aggregated data  $\bar{\mathbf{y}}^F$  is the sufficient statistics for model (8) of all the parameters and the discrepancy function in model (8). However, when  $\sigma_0^2$  is unknown, the sufficient statistics of model (8) is  $(\bar{\mathbf{y}}^F, s^2)$ , where  $s^2 = \sum_{l=1}^k \sum_{i=1}^n (y_l(\mathbf{x}_i) - \bar{y}^F)^2$ , with  $\bar{y}^F = \frac{1}{n} \sum_{i=1}^n \bar{y}^F(\mathbf{x}_i)$  [8]. Note the usual unbiased estimator of  $\sigma_0^2$  based on the full data is the sample variance  $s^2/(nk-1)$ , which has the variance  $\sigma_0^4/(nk-1)$  in estimating  $\sigma_0^2$ . However, the sample variance of  $\sigma_0^2$  based on the aggregated data is  $k(\bar{y}^F(\mathbf{x}_i) - \bar{y}^F)^2/(n-1)$ , where the variance of this estimator is  $\sigma_0^4/(n-1)$ , much larger than the sample variance based on full data when  $k$  is large. Thus, using the aggregated data in (13) is typically less efficient in estimating  $\sigma_0^2$  than the model of the full data in (8).

When the field data contain measurement bias and different mean parameters modeled as in (2), the sampling model of the aggregated data is

$$\bar{y}^F(\mathbf{x}) = f^M(\mathbf{x}, \boldsymbol{\theta}) + \delta(\mathbf{x}) + \frac{1}{k} \sum_{l=1}^k \mu_l + \frac{1}{k} \sum_{l=1}^k \delta_l(\mathbf{x}) + \frac{1}{k} \sum_{l=1}^k \epsilon_l. \quad (11)$$

The lemma below gives the marginal distributions of the aggregated data for both model (2) and model (8) of the full data.

**Lemma 4.** *1. Assuming the model (2) of the full data, after integrating out  $\boldsymbol{\delta}$  and  $\delta_l$ ,  $l = 1, \dots, k$ , the marginal distribution of  $\bar{\mathbf{y}}^F := (\bar{y}^F(\mathbf{x}_1), \dots, \bar{y}^F(\mathbf{x}_n))$  follows*

$$(\bar{\mathbf{y}}^F \mid \{\sigma_l^2, \mathbf{R}_l, \sigma_{0l}^2, \mu_l\}_{l=1}^k, \boldsymbol{\theta}, \tau^2, \mathbf{R}) \sim \text{MN} \left( \mathbf{f}_{\boldsymbol{\theta}}^M + \frac{1}{k} \sum_{l=1}^k \mu_l \mathbf{1}_n, \frac{1}{k^2} \sum_{l=1}^k \tilde{\Sigma}_l + \tau^2 \mathbf{R} \right). \quad (12)$$

where  $\tilde{\Sigma}_l = \sigma_l^2 \mathbf{R}_l + \sigma_{0l}^2 \mathbf{I}_n$  is defined in Lemma 1.

2. Assuming the model (8) of the full data, the marginal distribution of  $\bar{\mathbf{y}}^F$  follows

$$(\bar{\mathbf{y}}^F \mid \sigma_0^2, \mu, \boldsymbol{\theta}, \tau^2, \mathbf{R}) \sim \text{MN} \left( \mathbf{f}_{\boldsymbol{\theta}}^M + \mu \mathbf{1}_n, \frac{\sigma_0^2}{k} \mathbf{I}_n + \tau^2 \mathbf{R} \right). \quad (13)$$

Lemma 4 follows trivially by the law of the total expectation and total variance so the proof is omitted here. The theorem below connects the limiting distribution of the stack image in (9) and in (12), which is a direct consequence of Lemma 4.

**Theorem 2.** Assume  $\lim_{k \rightarrow \infty} \frac{1}{k} \sum_{l=1}^k \mu_l = \mu < \infty$ ,  $\sigma_0^2 < \infty$  and  $\lim_{k \rightarrow \infty} \frac{1}{k} \sum_{l=1}^k \tilde{\Sigma}_l < \infty$ . When  $k \rightarrow \infty$ , the limiting distribution of  $\bar{\mathbf{y}}^F$  in both (12) and in (13) follows

$$(\bar{\mathbf{y}}^F \mid \mu, \boldsymbol{\theta}, \tau^2, \mathbf{R}) \sim \text{MN} (\mathbf{f}_{\boldsymbol{\theta}}^M + \mu \mathbf{1}_n, \tau^2 \mathbf{R}). \quad (14)$$

### 3 Modeling the measurement bias and model discrepancy

In this section, we discuss the statistical models of the discrepancy function and measurement bias functions. We first introduce the Gaussian stochastic process in Section 3.1. We then present an example demonstrating the identifiability problem of the estimated calibration parameter in the GaSP model. A new stochastic process, called the discretized scaled Gaussian stochastic process, is introduced in Section 3.2 for the model discrepancy and for reducing the identifiability problem.

#### 3.1 Gaussian stochastic process

Let us first consider modeling the measurement bias  $\delta_l(\cdot)$  via a Gaussian stochastic process (GaSP)

$$\delta_l(\cdot) \sim \text{GaSP}(0, \sigma_l^2 K_l(\cdot, \cdot)), \quad (15)$$

where  $K_l(\cdot, \cdot)$  is the kernel function for  $l = 1, \dots, k$ , meaning that for any  $\{\mathbf{x}_1, \dots, \mathbf{x}_n\}$ , the marginal distribution of  $\boldsymbol{\delta}$  follows a multivariate normal distribution in (3), for  $l = 1, \dots, k$ .

For any inputs  $\mathbf{x}_a := (x_{a1}, \dots, x_{ap})$  and  $\mathbf{x}_b := (x_{b1}, \dots, x_{bp})$ , the covariance is typically assumed to have a product form in calibration

$$K_l(\mathbf{x}_a, \mathbf{x}_b) = \prod_{t=1}^p K_{l,t}(x_{at}, x_{bt}), \quad (16)$$

where each  $K_{l,t}(\cdot, \cdot)$  is a one-dimensional kernel function for correlation between the  $t^{\text{th}}$  coordinate of any two inputs for the source  $l$ ,  $l = 1, \dots, k$ . Denote  $d_t = |x_{at} - x_{bt}|$ . One popular choice of the correlation function is the power exponential correlation,  $K_{l,t}(d_t) = \exp\{- (d_t/\gamma_t)^{\alpha_t}\}$  with a roughness parameter  $\alpha_t$  typically held fixed and an unknown range parameter  $\gamma_t$  for the  $t^{\text{th}}$  coordinate of the input,  $t = 1, \dots, p$ . Another popular choice is the Matérn correlation. The Matérn correlation with the roughness parameter  $\alpha_t = (2k + 1)/2$  for  $k \in \mathbb{N}$  has a closed form expression. For example, the Matérn correlation function with  $\alpha_t = 5/2$  is as follows:

$$K_{l,t}(d_t) = \left( 1 + \frac{\sqrt{5}d_t}{\gamma_t} + \frac{5d_t^2}{3\gamma_t^2} \right) \exp\left( -\frac{\sqrt{5}d_t}{\gamma_t} \right). \quad (17)$$

A desirable feature of the Matérn correlation is that the sample path of the process is  $\lfloor \alpha_l \rfloor$  differentiable. More advantages of using (17) are discussed in [21]. In relation to the present scientific goal, we also note that previous works have argued that Matérn correlation functions are suitable for modeling atmospheric noise in InSAR data [29]. However, we do not limit ourselves to any specific correlation function and the methods discussed in this work apply to all such functions.

In [28], the discrepancy function is also modeled as a GaSP:

$$\delta(\cdot) \sim \text{GaSP}(0, \tau^2 K(\cdot, \cdot)), \quad (18)$$

where  $K(\cdot, \cdot)$  is a kernel function modeling the correlation between two inputs. The identifiability issue, however, has been widely observed in modeling spatially correlated data, where the spatial random effect was confounded with a linear fixed effect, i.e.  $f^M(\mathbf{x}, \boldsymbol{\theta})$  being a linear model of  $\boldsymbol{\theta}$ , [24, 44]. These pioneering studies show that the estimated parameters in the fixed effect can change dramatically, depending whether or not to include a term to model the spatial correlation.

In a calibration task, the identifiability of the calibration parameters was also found to be a problem when the discrepancy function is modeled by a GaSP [6, 50, 53]. It was not noticed that the usual estimator of the calibration parameters, such as the maximum likelihood estimator, is typically not even consistent when the discrepancy function is modeled by a GaSP. Here we provide a closed-form example to understand the identifiability problem.

**Example 1.** Assume field data of the source  $l$  at input  $x_i$  follows

$$y_l^F(x_i) = f^M(x_i, \theta) + \delta(x_i) + \epsilon_l,$$

where  $f^M(x_i, \theta) = \theta$ ,  $\delta(\cdot) \sim \text{GaSP}(0, \tau^2 K(\cdot, \cdot))$ , with  $K(x_i, x_j) = \exp(-|x_i - x_j|/\gamma)$ , and  $\epsilon_l \sim N(0, \sigma_0^2)$  is an independent Gaussian noise for each  $x_i$ ,  $i = 1, \dots, n$ , and for  $l = 1, \dots, k$ . Assume the observations  $y_l^F(x_i)$  are equally spaced from  $[0, 1]$ , i.e.  $x_i = (i - 1)/(n - 1)$ , for  $i = 1, \dots, n$  and  $l = 1, \dots, k$ . Further assume  $\gamma$ ,  $\tau^2$  and  $\sigma_0^2$  are known and finite. The task is to estimate  $\theta$ .

The following lemma shows that the maximum likelihood estimator (MLE) is inconsistent when both  $n$  and  $k$  go to infinity in Example 1.

**Lemma 5.** Assume  $\tau^2 > 0$  and  $\gamma > 0$  are both finite. When  $n \rightarrow \infty$  and  $k \rightarrow \infty$ , after marginalizing out  $\boldsymbol{\delta}$ , the maximum likelihood estimator of  $\theta$  in Example 1 has the limiting distribution:

$$\hat{\theta}_{MLE} \sim N\left(\theta, \frac{2\tau^2\gamma}{2\gamma + 1}\right). \quad (19)$$

Lemma 5 means that even if one has infinite repeated experiments and infinite observations in a fixed input domain in each experiment, the asymptotic distribution of the MLE of the calibration parameter, defined as the mean parameter in this example, is inconsistent, if the discrepancy function is assumed to be a GaSP with the exponential kernel. This result is surprising but reasonable, because the discrepancy function is shared across all experiments. No matter how many experiments we have, the shared discrepancy function contained in each experiment does not change. Since the MLE of the calibration parameters in model (8) based on the individual sources of data and aggregated data is the same implied by Lemma 3, one only needs to consider the limiting case where one has one source of data with noise-free observations. We therefore present the following remark, which is a direct consequence of the proof of Lemma 5.

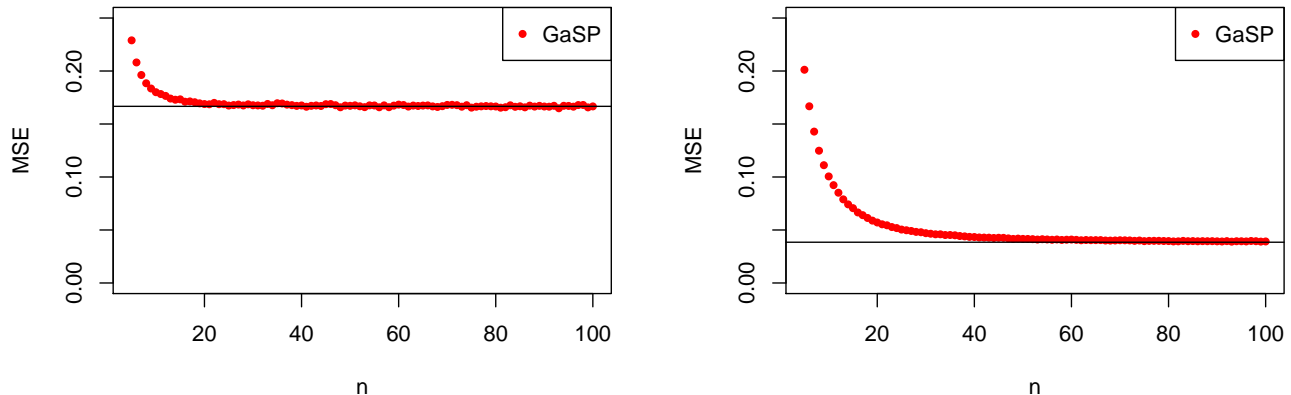


Figure 2: Mean squared errors of the MLE of  $\theta$  in Example 1 for different numbers of observations when  $k \rightarrow \infty$ . The limiting variance of the MLE for GaSP data in Lemma 5 is graphed as the black horizontal lines.  $10^5$  simulations are implemented to calculate each value. The range parameter is assumed to be  $\gamma = 0.1$  and  $\gamma = 0.02$  in the left and right panels, respectively, both assuming  $\tau^2 = 1$ .

**Remark 1.** *If one has one source of noise-free experimental observations, i.e.,  $y_i^F(x_i) = \theta + \delta(x_i)$ , for  $i = 1, \dots, n$ , where  $\delta(\cdot)$  follows a GaSP with the covariance function  $\tau^2 K(x_i, x_j) = \tau^2 \exp(-|x_i - x_j|/\gamma)$  for any  $1 \leq i, j \leq n$ . When  $n \rightarrow \infty$ , the limiting distribution of the maximum likelihood estimator of  $\theta$  follows (19).*

The MSE of the MLE of  $\theta$  in Example 1 is graphed as the red triangles at different number of observations in Figure 2 when  $k \rightarrow \infty$ . In the left panel, when  $\gamma = 0.1$ , the MSE quickly converges when the sample size increases. In the right panel, the MSE converges to a smaller value when  $\gamma = 0.02$ , because the correlation is smaller. Both MSEs converge to the limiting value,  $\frac{2\tau^2\gamma}{2\gamma+1}$ , found in Lemma 5.

The results in Lemma 5 and Remark 1 are both examples of the equivalency of the Gaussian measures. Although the closed-form expression of the limiting distribution of the MLE of the calibration parameter in Lemma 5 relies on the exponential kernel function. The MLE is inconsistent for the mean parameter of the GaSP model with many other kernel functions, such as the Matérn kernel. We refer the reader to Chapter 4.2 in [48] for the detailed discussion in this topic.

Many attempts have been made to identify discrepancy function and calibration parameters. In [50], the optimal estimator of the calibration parameter is defined to be the one that minimizes the  $L_2$  loss between the mathematical model and reality

$$L_2(\boldsymbol{\theta}) = \int_{\mathbf{x} \in \mathcal{X}} (y^R(\mathbf{x}) - f^M(\mathbf{x}, \boldsymbol{\theta}))^2 d\mathbf{x}. \quad (20)$$

Indeed, in mathematical model calibration, one hopes the variability in the field data to be explained by the estimated calibration parameters in mathematical model, rather than by the discrepancy function, as the calibration parameters often have practical meanings. It is thus sensible

to argue that, if the trend and intercept are properly modeled in the mathematical model, a calibrated mathematical model that fits closely the reality is more likely to be true than another mathematical model that is far from the reality, in terms of the  $L_2$  loss. However, the estimated calibration parameters in the GaSP model typically do not converge to the one that minimizes the  $L_2$  loss in (20) [22, 50].

When the discrepancy function is modeled by a GaSP, the  $L_2$  loss between the mathematical model and reality can be expressed as  $L_2(\boldsymbol{\theta}) = \int_{\mathbf{x} \in \mathcal{X}} \delta^2(\mathbf{x}) d\mathbf{x}$ , a random variable whose measure is induced by the GaSP. The distribution of this random  $L_2$  loss often has too much probability mass at large values, when the correlation is large in a GaSP model. Because of this reason, a new stochastic process for the discrepancy function, called the scaled Gaussian stochastic process, was introduced in [20] and [22], which assigns more probability mass at the region with smaller values than the one induced by GaSP. We introduce a computationally feasible version of this process, called the discretized scaled Gaussian stochastic process in the Section 3.2.

### 3.2 Discretized scaled Gaussian stochastic process

Consider the discretized scaled Gaussian stochastic process (S-GaSP) for modeling the discrepancy function:

$$\delta_z(\mathbf{x}) = \left\{ \delta(\mathbf{x}) \mid \frac{1}{n} \sum_{i=1}^n \delta^2(\mathbf{x}_i) = Z \right\}, \quad (21)$$

$$\delta \sim \text{GaSP}(0, \tau^2 K(\cdot, \cdot)), \quad Z \sim p_{\delta_z}(\cdot),$$

where  $p_{\delta_z}(\cdot)$  is a density function of the squared error between the reality and mathematical model at the observed inputs. Given  $Z = z$ , S-GaSP is a GaSP constrained at the space  $\sum_{i=1}^n \frac{\delta^2(\mathbf{x}_i)}{n} = z$ . The idea is to assign more probability mass on the smaller squared error by  $p_{\delta_z}(\cdot)$  defined later.

Denote  $p_\delta(Z = z \mid \boldsymbol{\gamma}, \tau^2)$  the density of  $Z = z$  induced by the GaSP model in (18), where  $\tau^2$  and  $\boldsymbol{\gamma}$  are the variance parameter and range parameters in the covariance function, respectively. We let  $p_{\delta_z}(\cdot)$  proportional to  $p_\delta(\cdot)$ , but scaled by a non-increasing function:

$$p_{\delta_z}(Z = z \mid \boldsymbol{\gamma}, \tau^2, \lambda_z) = \frac{f_Z(Z = z \mid \tau^2, \lambda_z) p_\delta(Z = z \mid \boldsymbol{\gamma}, \tau^2)}{\int_0^\infty f_Z(Z = t \mid \tau^2, \lambda_z) p_\delta(Z = t \mid \boldsymbol{\gamma}, \tau^2) dt}, \quad (22)$$

where  $f_Z(Z = z \mid \tau^2, \lambda_z)$  is a non-increasing scaling function depending on  $\tau^2$  and scaling parameter  $\lambda_z$ , at all  $z \geq 0$ . For computational reasons, the default choice of  $f_Z(\cdot)$  is an exponential distribution

$$f_Z(Z = z \mid \tau^2, \lambda_z) = \frac{\lambda_z}{2\tau^2 \text{Vol}(\mathcal{X})} \exp\left(-\frac{\lambda_z z}{2\tau^2 \text{Vol}(\mathcal{X})}\right), \quad (23)$$

where  $\lambda_z$  is a positive scaling parameter and  $\text{Vol}(\mathcal{X})$  is the volume of the input domain  $\mathcal{X}$ .

It is easy to see that GaSP is a special case of S-GaSP when  $f_Z(\cdot)$  is a constant function, or equivalently  $\lambda_z = 0$ . On the other hand, starting from a GaSP model with any reasonable covariance function  $\tau^2 K(\cdot, \cdot)$ , after marginalizing out  $Z$ , it was shown in [20] that the marginal distribution of  $\boldsymbol{\delta}_z := (\delta_z(\mathbf{x}_1), \dots, \delta_z(\mathbf{x}_n))^T$  follows a multivariate normal distribution with a transformed covariance matrix:

$$\boldsymbol{\delta}_z \mid \boldsymbol{\Theta} \sim \text{MN}(\mathbf{0}, \tau^2 \mathbf{R}_z), \quad (24)$$

Table 1: Predictive mean squared errors and the MLE of the parameters in GaSP and S-GaSP calibration models in Example 2.

	$\text{MSE}_{f^M}$	$\text{MSE}_{f^{M+\delta}}$	$\hat{\boldsymbol{\theta}}$	$\hat{\tau}^2$	$\hat{\gamma}$	$\hat{\sigma}_0^2$
GaSP	91.5	$6.12 \times 10^{-3}$	(13.2, 1.90)	$1.32 \times 10^2$	(1.44, 1.8)	$1.76 \times 10^{-3}$
S-GaSP	1.58	$5.47 \times 10^{-3}$	(3.76, 2.01)	$3.54 \times 10^2$	(1.72, 2.13)	$1.74 \times 10^{-3}$

where

$$\mathbf{R}_z = \left( \mathbf{R}^{-1} + \frac{\lambda}{n} \mathbf{I}_n \right)^{-1}, \quad (25)$$

with the  $(i, j)$ th term of  $\mathbf{R}$  being  $K(\mathbf{x}_i, \mathbf{x}_j)$ .

Theoretical and computational properties of S-GaSP, such as the orthogonality sequence representation, convergence rates and predictive distributions, are studied extensively in [22], where the scaled parameter  $\lambda_z$  was shown to be the weight between the penalty of  $L_2$  norm and the native norm of the model discrepancy in the S-GaSP calibration. A larger  $\lambda_z$  assigns more prior probability on the smaller  $L_2$  norm of the discrepancy function. Under some regularity conditions, a suitable choice of  $\lambda_z$  guarantees the predictive distribution in the S-GaSP model converges to the reality as fast as in the GaSP model, and the estimation of the calibration parameters in the S-GaSP model also minimizes the  $L_2$  loss between the reality and mathematical model, when the sample size goes to infinity. Thus, we follow [22] to let  $\lambda_z = C\sqrt{n}$ , with  $C = 100$ .

We present one example to illustrate the difference between the GaSP and S-GaSP calibrations.

**Example 2.** Assume  $y^F(\mathbf{x}) = y^R(\mathbf{x}) + \epsilon$  where  $\mathbf{x} = (x_1, x_2) \in [0, 1]^2$ ,  $\epsilon \sim N(0, 0.05^2)$  is an independent Gaussian noise for each  $\mathbf{x}$  and reality is assumed to be a function in [30]:

$$y^R(\mathbf{x}) = \frac{1}{6} \{ (30 + 5x_1 \sin(5x_1))(4 + \exp(-5x_2)) - 100 \}.$$

Assume  $f^M(\mathbf{x}, \boldsymbol{\theta}) = \theta_1 + \theta_2 \sin(5x_1)$ , where  $\boldsymbol{\theta} = (\theta_1, \theta_2)$  are two unknown calibration parameters. The field data  $y^F(\mathbf{x}_i)$  is observed at  $\mathbf{x}_i$ ,  $i = 1, \dots, 30$ , drawn from the maximin Latin hypercube design [45]. The goal is to estimate  $\boldsymbol{\theta}$  and predict the reality at all  $\mathbf{x} \in [0, 1]^2$ .

For Example 2, the true values of the calibration parameters are not well-defined because of the presence of a deterministic discrepancy function. We thus compare the GaSP and S-GaSP models of the discrepancy function by their predictive performance based on two criteria. The first criterion is to use only the calibrated mathematical model to predict the reality, and the second one is to use both the calibrated mathematical model and discrepancy function for predictions.

We evaluate the predictions on  $y^R(\mathbf{x}_i^*)$  at the held-out  $\mathbf{x}_i^*$ , uniformly sampled from  $[0, 1]^2$  for  $i = 1, \dots, 1000$ . Denote  $\text{MSE}_{f^M}$  the predictive mean squared error using only the calibrated mathematical model and denote  $\text{MSE}_{f^{M+\delta}}$  the predictive mean squared error using both the calibrated mathematical model and the discrepancy function for prediction:

$$\text{MSE}_{f^M} = \frac{\sum_{i=1}^{n^*} (f^M(\mathbf{x}_i^*, \hat{\boldsymbol{\theta}}) - y^R(\mathbf{x}_i^*))^2}{n^*} \quad \text{and} \quad \text{MSE}_{f^{M+\delta}} = \frac{\sum_{i=1}^{n^*} (\hat{y}^R(\mathbf{x}_i^*) - y^R(\mathbf{x}_i^*))^2}{n^*},$$

where  $\hat{y}^R(\mathbf{x}_i^*)$  is the predictive mean at  $\mathbf{x}_i^*$  by the calibrated mathematical model and discrepancy function.

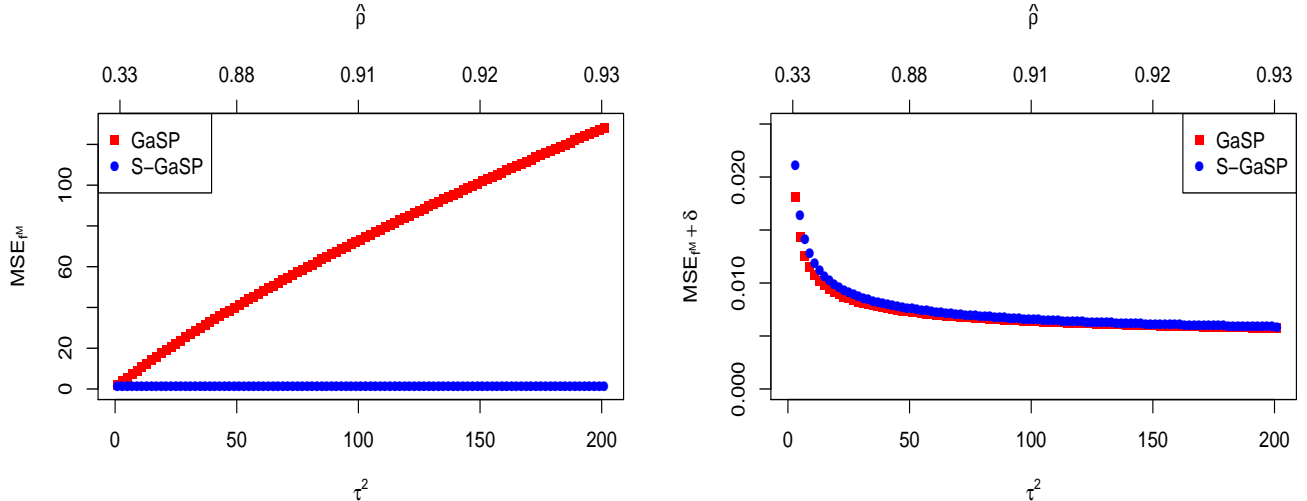


Figure 3: Predictive mean squared errors of Example 2 when  $\tau^2$  is fixed in the GaSP and S-GaSP calibrations. The  $\text{MSE}_{f_M}$  and  $\text{MSE}_{f_M+\delta}$  are shown in the left and right panel, respectively. The upper x coordinate is the estimated median value of the correlation matrix  $\mathbf{R}$  for each  $\tau^2$  in the GaSP calibration model.

The out-of-sample predictions using the GaSP and S-GaSP calibrations are provided in Table 1, where the parameters are estimated by the MLE via the low-storage quasi-Newton optimization method [39] with 10 different initializations. The  $\text{MSE}_{f_M+\delta}$  is similar using both GaSP and S-GaSP calibration models, while the  $\text{MSE}_{f_M}$  by S-GaSP is much smaller than the one by GaSP.

Denote  $\rho$  the median value in the correlation matrix  $\mathbf{R}$  and let  $\hat{\rho}$  be the estimated value in the GaSP calibration model. After plugging in the estimated range parameters  $\hat{\gamma}$  in Table 1, we found  $\hat{\rho} \approx 0.92$ , indicating relatively large estimated correlation. To further explore the cause of the large mean squared error in the GaSP calibration using the calibrated mathematical model, we fix the scale parameter  $\tau^2$  at different values and estimate the rest of the parameters by the MLE in the GaSP calibration. To further illustrate the difference, we use the same estimated parameters in the covariance matrix in the S-GaSP calibration, and estimate the calibration parameters by the MLE. The  $\text{MSE}_{f_M}$  and  $\text{MSE}_{f_M+\delta}$  due to the change of  $\tau^2$  are shown in Figure 3.

When  $\tau^2$  is fixed at a small value, the median estimated correlation in the GaSP calibration, shown in the upper x coordinate in Figure 3, is small. The  $\text{MSE}_{f_M}$  is small when the correlation is small, shown in the left panel in Figure 3. However, the  $\text{MSE}_{f_M+\delta}$  is comparatively large in this scenario, shown in the right panel. When  $\tau^2$  is fixed at a large value, the estimated correlation is large. The  $\text{MSE}_{f_M+\delta}$  becomes small by both models. However, the  $\text{MSE}_{f_M}$  becomes incredibly large by the GaSP model due to the large estimated correlation, whereas the  $\text{MSE}_{f_M}$  is still very small in the S-GaSP model, shown in the left panel in Figure 3.

Example 2 shows that the calibrated mathematical model can be far from the reality in the GaSP model, when the estimated correlation is large. When the correlation is small, the predictive distribution of the mathematical model and discrepancy function may sometimes be less precise to predict the reality as the one with a large correlation. In comparison, the calibrated mathematical model by the S-GaSP calibration is still close to the reality when the correlation is large. Thus the small  $\text{MSE}_{f_M}$  and  $\text{MSE}_{f_M+\delta}$  may not be simultaneously obtained in the GaSP model, but they can be achieved at the same time in the S-GaSP calibration.

Table 2: Input variables, calibration parameters of the geophysical model and other model parameters in calibration.

Input variables ( $\mathbf{x}$ )	Description
$x_1$	East-west spatial coordinate
$x_2$	North-south spatial coordinate
Calibration parameters ( $\boldsymbol{\theta}$ )	Description
$\theta_1 \in [-2000, 3000]$	Spatial coordinate of east-west chamber position ( $m$ )
$\theta_2 \in [-2000, 5000]$	Spatial coordinate of north-south chamber position ( $m$ )
$\theta_3 \in [500, 6000]$	Depth of the chamber ( $m$ )
$\theta_4 \in [0, 0.15]$	Volume change rate of the reservoir ( $m^3/s$ )
$\theta_5 \in [0.25, 0.33]$	Poisson's ratio (host rock property)
Model parameters	Description
$\boldsymbol{\mu} = (\mu_1, \dots, \mu_k)$	mean parameters
$\boldsymbol{\beta}_{1:k} = (\beta_{1,1}, \dots, \beta_{1,p}, \dots, \beta_{k,1}, \dots, \beta_{k,p})$	inverse range parameters of the measurement bias
$\boldsymbol{\eta} = (\eta_1, \dots, \eta_k)$	nugget parameters of the measurement bias
$\boldsymbol{\sigma}^2 = (\sigma_1^2, \dots, \sigma_k^2)$	scale parameters of the measurement bias
$\boldsymbol{\beta} = (\beta_1, \dots, \beta_p)$	range parameters of the model discrepancy
$\tau^2$	scale parameter of the model discrepancy

## 4 Parameter estimation using multiple sources of data

In this section, we discuss the parameter estimation in calibration models. The S-GaSP model of the  $l$ th interferogram,  $l = 1, \dots, k$ , is defined below

$$\mathbf{y}_l^F(\mathbf{x}) = f^M(\mathbf{x}, \boldsymbol{\theta}) + \delta_z(\mathbf{x}) + \delta_l(\mathbf{x}) + \mu_l + \epsilon_l. \quad (26)$$

The only different between the S-GaSP calibration model in (26) and the GaSP calibration model in (2) is on the model of the discrepancy function, assumed to follow a discretized S-GaSP in (21) and a GaSP in (18), respectively. Note that the marginal distribution of the discretized S-GaSP is a multivariate normal distribution with the covariance matrix  $\tau^2 \mathbf{R}_z$  specified in (25). Thus, all the likelihoods and predictive distributions derived in Section 2.1 can be used in the S-GaSP calibration, only replacing  $\mathbf{R}$  by  $\mathbf{R}_z$ .

The parameters in (2) and (26) both contain the calibration parameters, mean parameters, variance parameters of noises, range and scale parameters of the model discrepancy function and measurement bias functions. For computational purposes, we transform the variance parameter  $\sigma_{0l}^2$  to define the nugget parameter  $\eta_l := \sigma_{0l}^2 / \sigma_l^2$ , for  $l = 1, \dots, k$ . By definition,  $\sigma_{0l}^2$  becomes the overall scale parameter of the matrix  $\tilde{\boldsymbol{\Sigma}}_l$  in Lemma 1 which has a conjugate prior that simplifies the computation. We also transform to define the inverse range parameter  $\beta_t = 1/\gamma_t$ , for  $t = 1, \dots, p$ , and  $\beta_{l,t} = 1/\gamma_{l,t}$ , for  $l = 1, \dots, k$  and  $t = 1, \dots, p$ .

The input variables, calibration parameters and other model parameters are listed in Table 2 for the calibrating the geophysical model for Kilauea Volcano using multiple interferograms. We assume the following objective prior for the calibration problem

$$\pi(\boldsymbol{\theta}, \boldsymbol{\mu}, \boldsymbol{\beta}_{1:k}, \boldsymbol{\eta}, \boldsymbol{\sigma}^2, \boldsymbol{\beta}, \tau^2) \propto \pi(\boldsymbol{\theta}) \frac{\pi^{JR}(\boldsymbol{\beta})}{\tau^2} \prod_{l=1}^k \left\{ \frac{\pi^{JR}(\boldsymbol{\beta}_l, \eta_l)}{\sigma_l^2} \right\}, \quad (27)$$

The prior of the calibration parameters  $\theta$  often depends on experts’ knowledge, as the calibration parameters have scientific meanings. For the problem of calibrating the geophysical model of Kīlauea Volcano, we assume  $\pi(\theta)$  a uniform distribution on the domain of the calibration parameters, listed in Table 2. The mean and scaled parameters are assigned a usual location-scale prior in (27), i.e.  $\pi(\tau^2) \propto 1/\tau^2$  and  $\pi(\mu_l, \sigma_l^2) \propto 1/\sigma_l^2$ , for  $l = 1, \dots, k$ . Furthermore, we assume the jointly robust (JR) prior for the range and nugget parameters in both the measurement bias functions and discrepancy function defined below

$$\pi^{JR}(\beta, \eta) = c \left( \sum_{t=1}^p C_t \beta_t + \eta \right)^a \exp \left\{ -b \left( \sum_{t=1}^p C_t \beta_t + \eta \right) \right\},$$

where  $c = \frac{p! b^{a+p+1} \prod_{t=1}^p C_t}{\Gamma(a+p+1)}$  is a normalizing constant;  $a > -1 - p$ ,  $b > 0$  and  $C_t > 0$  are prior parameters. We assume the default prior parameters:  $a = 1/2 - p$ ,  $b = 1$  and  $C_t = n^{-1/p} |x_t^{max} - x_t^{min}|$ , where  $x_t^{max}$  and  $x_t^{min}$  are the maximum and minimum values of the input at the  $t$ th coordinate,  $t = 1, \dots, p$ . The advantages of using the JR prior in calibration is studied in [17].

The geophysical model used in this study is computationally inexpensive, but that is often not the case [2]. In such cases, a statistical emulator may be used to approximate the geophysical model based on a limited set of model runs on some prespecified inputs. We refer the reader to [21] for an extensive discussion of the robust parameter estimation of the emulator.

We implemented the full Bayesian analysis of calibration and prediction using both the GaSP and discretized S-GaSP discrepancy models in an R package, called “RobustCalibration”, available on CRAN ([18]). The package allows for both single source and multiple sources of data. The Robust GaSP emulator introduced in [17, 21] is combined in the “RobustCalibration” package for use when the mathematical model is computationally expensive. Although we focus on using satellite interferograms for calibration, the methodology and the R package provide a general statistical framework for combining multiple sources of data for calibration and prediction.

## 4.1 Downsampling satellite interferograms

A single InSAR image is often composed of hundreds of thousands of pixels. Even for very simple geophysical models, the expense of computing deformation at all these points can quickly become prohibitive, and subsampling techniques are typically employed. One simple approach is to uniformly sample a subset of pixels (with or without averaging of nearby pixels) and use the output values on these pixels in the calibration and prediction [20, 43]. We found that often the posterior distributions of the calibration parameters become stable with only a few hundred pixels.

Quadtree-type algorithms are a more sophisticated approach to downsampling. In these approaches, groups of pixels are averaged together (the median can also be used) into “boxes” whose sizes are based on gradients in the image [27, 46], the resolution of the forward model [31], or characteristics of both the data and model [51]. These algorithms have become widely used for InSAR processing when used in model calibration and prediction [e.g. 7, 38].

Because the boxes (“pixels”) in a quadtree-processed image, such as in Figure 1d, are computed from different numbers of pixels, in a calibration problem it is therefore important to take into account the size of the quadtree boxes to avoid over-representing regions with a high point density [31, 46, 49]. This seems to have been overlooked in many previous studies using quadtree-processed

InSAR data for model calibration and prediction.

Consider the calibration model with one source of data and no measurement bias, i.e.  $y^F(\mathbf{x}) \sim N(f^M(\mathbf{x}, \boldsymbol{\theta}) + \delta(\mathbf{x}) + \mu, \sigma_0^2)$ . The density of  $\mathbf{y}^F = (y^F(\mathbf{x}_1), \dots, y^F(\mathbf{x}_n))^T$  is

$$p(\mathbf{y}^F \mid \boldsymbol{\theta}, \sigma_0^2, \boldsymbol{\delta}) = \frac{1}{(2\pi\sigma_0^2)^{n/2}} \exp\left(-\sum_{i=1}^n \frac{(y^F(\mathbf{x}_i) - f^M(\mathbf{x}_i, \boldsymbol{\theta}) - \delta(\mathbf{x}_i))^2}{2\sigma_0^2}\right). \quad (28)$$

Suppose we have  $J$  boxes on  $n$  pixels of the quadtree image, each box having the size  $n_j$ , for  $j = 1, \dots, J$ . Let  $\mathbf{y}^{F,Q} = \{y^{F,Q}(\mathbf{x}_{S_1}), \dots, y^{F,Q}(\mathbf{x}_{S_J})\}$  denote output in a quadtree-processed image, where  $S_j$  is the set of indices contained in the  $j$ th box in the quadtree image,  $j = 1, \dots, J$ . Further let  $f^{M,Q}(\mathbf{x}_{S_j}, \boldsymbol{\theta})$ ,  $j = 1, \dots, J$ , and  $\boldsymbol{\delta}^Q := (\delta^Q(\mathbf{x}_{S_1}), \dots, \delta^Q(\mathbf{x}_{S_J}))^T$  denote the corresponding outputs of the mathematical model and discrepancy function in the quadtree-processed image, respectively. Consider the following weighted likelihood

$$p(\mathbf{y}^{F,Q} \mid \boldsymbol{\theta}, \sigma_0^2, \boldsymbol{\delta}^Q) = \frac{1}{(2\pi\sigma_0^2)^{n/2}} \exp\left(-\sum_{j=1}^J w_j \frac{(y^{F,Q}(\mathbf{x}_{S_j}) - f^{M,Q}(\mathbf{x}_{S_j}, \boldsymbol{\theta}) - \delta^Q(\mathbf{x}_{S_j}))^2}{2\sigma_0^2}\right). \quad (29)$$

It is obvious that form (28) and form (29) are equivalent if the weight  $\{w_j\}_{j=1}^J$  is chosen to satisfy

$$\sum_{i \in S_j} (y^F(\mathbf{x}_i) - f^M(\mathbf{x}_i, \boldsymbol{\theta}) - \delta(\mathbf{x}_i))^2 = w_j (y^{F,Q}(\mathbf{x}_{S_j}) - f^{M,Q}(\mathbf{x}_{S_j}, \boldsymbol{\theta}) - \delta^Q(\mathbf{x}_{S_j}))^2. \quad (30)$$

for  $j = 1, \dots, J$ . In general, equation (30) is hard to enforce in practice, as one does not know the discrepancy function a priori. Some previous weighting schemes utilize the estimated covariance structure of the InSAR data [31, 49]. The weight  $w_j \propto n_j$  was previously suggested in [46], and used in [3, 4] for  $j = 1, \dots, J$ . Compared to the calibration using the quadtree image without any weighting (or i.e.  $w_j = 1$ ),  $w_j \propto n_j$  seems to provide a simple fix to the bias caused by the size of the boxes in the quadtree image. The theoretical justification of the weighting scheme of the quadtree-processed images is an open question.

Another issue using the quadtree-processed images is that of identifying the measurement bias and model discrepancy requires aligned measurements (measurements taken at the same spatial points), whereas the quadtree algorithm typically produces images with misaligned inputs, which may cause the computation operations of the likelihood and predictive distributions by Lemma 1 and Theorem 1 to increase from  $O(kn^3)$  to  $O((kn)^3)$ , for  $k$  images each with  $n$  points. Both downsampling schemes will be compared in Section 5.2.

## 5 Numerical results

### 5.1 Simulation study

We first study a simulated example below.

**Example 3.** Assume the data is sampled from model (2), where  $f^M(x, \theta) = \sin(\theta x)$  with  $\theta = \pi/2$ . The model discrepancy and measurement bias are assumed to follow (3) and (4), respectively, where  $\sigma = 0.2$  and  $\sigma_l = 0.4 + 0.4(l-1)/(k-1)$ , with  $\mathbf{R}$  and  $\mathbf{R}_l$  both parameterized by the Matérn

kernel in (17) with  $\gamma = 0.1$  and  $\gamma_l = 0.02$ , respectively, for  $l = 1, \dots, k$ . The standard deviation of the noise is  $\sigma_{0l}^2 = 0.05$  and  $y_l^F(x_i)$  is observed equally spaced at  $x_i \in [0, 1]$  for  $i = 1, \dots, n$  and  $l = 1, \dots, k$ . We let  $n = 100$  and implement  $N = 200$  experiments at three configurations with  $k = 5$ ,  $k = 10$  and  $k = 15$ .

In Example 3, the GaSP calibration model is the true sampling model, as both the discrepancy function and the measurement bias are sampled from the GaSPs with Matérn kernel functions. In practice, some sources have bigger measurement bias than the others so we assume the variance of the measurement bias is different in Example 3. Here we compare three models. The first and second approaches are the GaSP calibration and S-GaSP calibration based on the full data, where the discrepancy function is modeled by the GaSP in (18) and the discretized S-GaSP model in (21), respectively, both with the Matérn kernel function in (17). The measurement bias functions are assumed to follow GaSPs in both models. Also included is the GaSP calibration model based on the aggregated data, i.e. the average value of all sources of data at each  $x_i$ ,  $i = 1, \dots, n$ .

The unknown parameters of the GaSP calibration and S-GaSP calibration models using the full data are  $(\theta, \sigma^2, \{\sigma_l^2, \beta_l, \eta_l\}_{l=1}^k)$ , where  $\beta_l = 1/\gamma_l$  and  $\eta_l = \sigma_{0l}^2/\sigma_l^2$  are the inverse range parameter and the nugget parameter, respectively, for  $l = 1, \dots, k$ . The unknown parameters of the GaSP calibration model based on the aggregated data are  $(\theta, \sigma^2, \beta, \eta)$ , where  $\beta = 1/\gamma$  and  $\eta = \sigma_0^2/\sigma^2$ . For each approach, we draw 20,000 posterior samples of the parameters, with the first 4,000 burn-in posterior samples in each experiment. We thin the Markov chain to reduce the autocorrelation between the posterior samples, and the samples in every 10th step are used for the analysis.

The measurement bias and observations of the first two sources of data, the model discrepancy and the reality in the first simulated experiment for  $k = 10$  in Example 3 are graphed in Figure 4, along with the estimations by the three approaches. All methods seem to capture the patterns of the measurement bias, model discrepancy and reality. The estimation by the GaSP calibration model and S-GaSP calibration models based on the full data are more accurate than the ones by the GaSP calibration using the aggregated data. This is because the true model contains the measurement bias and the variance of the noise is unknown. As discussed in Section 2.2, modeling the full data is thus more efficient than the one by the aggregated data in this scenario.

The mean square error (MSE) of measurement bias, discrepancy functions, reality and the squared error (SE) of the calibration parameter by different approaches for each experiment in Example 3 are shown in Figure 5. First, even though the data is sampled from the GaSP calibration model, the MSEs of the S-GaSP calibration and the GaSP calibration in estimation are similar. Second, both methods based on the full data are better than the GaSP calibration based on the aggregated data, as averaging different sources of data causes loss of information due to the presence of the measurement bias and the unknown noise parameter. The estimation of the calibration parameters by the three methods are similar. When the number of sources of data increases from 5 to 15, all methods become more accurate in estimating the measurement bias, discrepancy function, reality and calibration parameter. The decrease of SEs of the calibration parameter is slow when the number of sources of the observations increases, because of the relatively large variance and correlation in the measurement bias. The MSEs and SEs based on three approaches also get closer when the number of sources of data increases.

When the number of sources of the data goes to infinity, the limiting distribution based on the aggregated data in Example 3 is given in Theorem 2. We sample the data from the limiting distribution and compute the maximum likelihood estimator of the calibration parameter at different

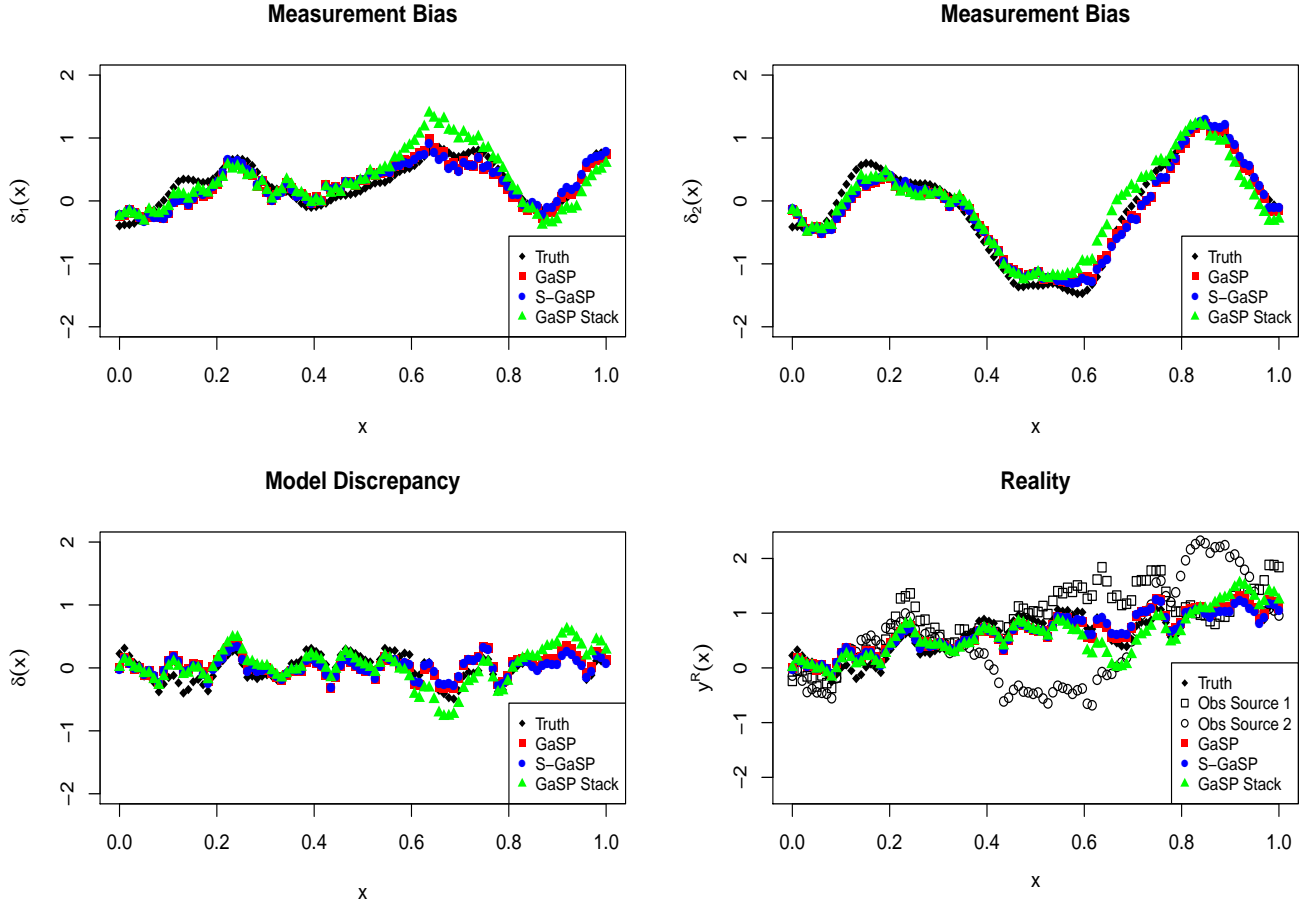


Figure 4: The measurement bias in the first two sources, the model discrepancy function and the reality in the first experiment of Example 3 when  $k = 10$  are graphed in the upper panels, lower left panel and lower right panel, respectively. The truth, the estimation by the GaSP and S-GaSP calibration based on the full data are graphed as the black diamonds, the red squares and blue dots, respectively. The estimation of the GaSP calibration based on aggregated data, denoted as GaSP Stack, is graphed as the green triangles. The observations from the first and second sources are graphed as black circles and black squares, respectively, in the lower right panel. The black diamonds, red squares and blue dots almost overlap in all panels.

sample sizes. We repeat 500 experiments and graph the average MSE of the maximum likelihood estimator of the calibration parameter in Figure 6. We consider two scenarios with  $\gamma = 0.02$  (the setting assumed in Example 3) and  $\gamma = 0.005$ . Comparing the left panel and the right panel in Figure 6, the average MSE is smaller when  $\gamma$  is smaller because measurement bias at different inputs is less correlated in this scenario. When the sample size increases, the MSE won't decrease to zero in both scenarios. The lower bound of the MSE in the left panel, however, is much smaller than the MSE we obtained using  $k = 15$  sources of data, shown in lower right panel in Figure 5. Thus, when more sources of data are available, the estimation of the calibration parameters will typically become more accurate.

Example 3 indicates that we are able to separate the measurement bias functions and model

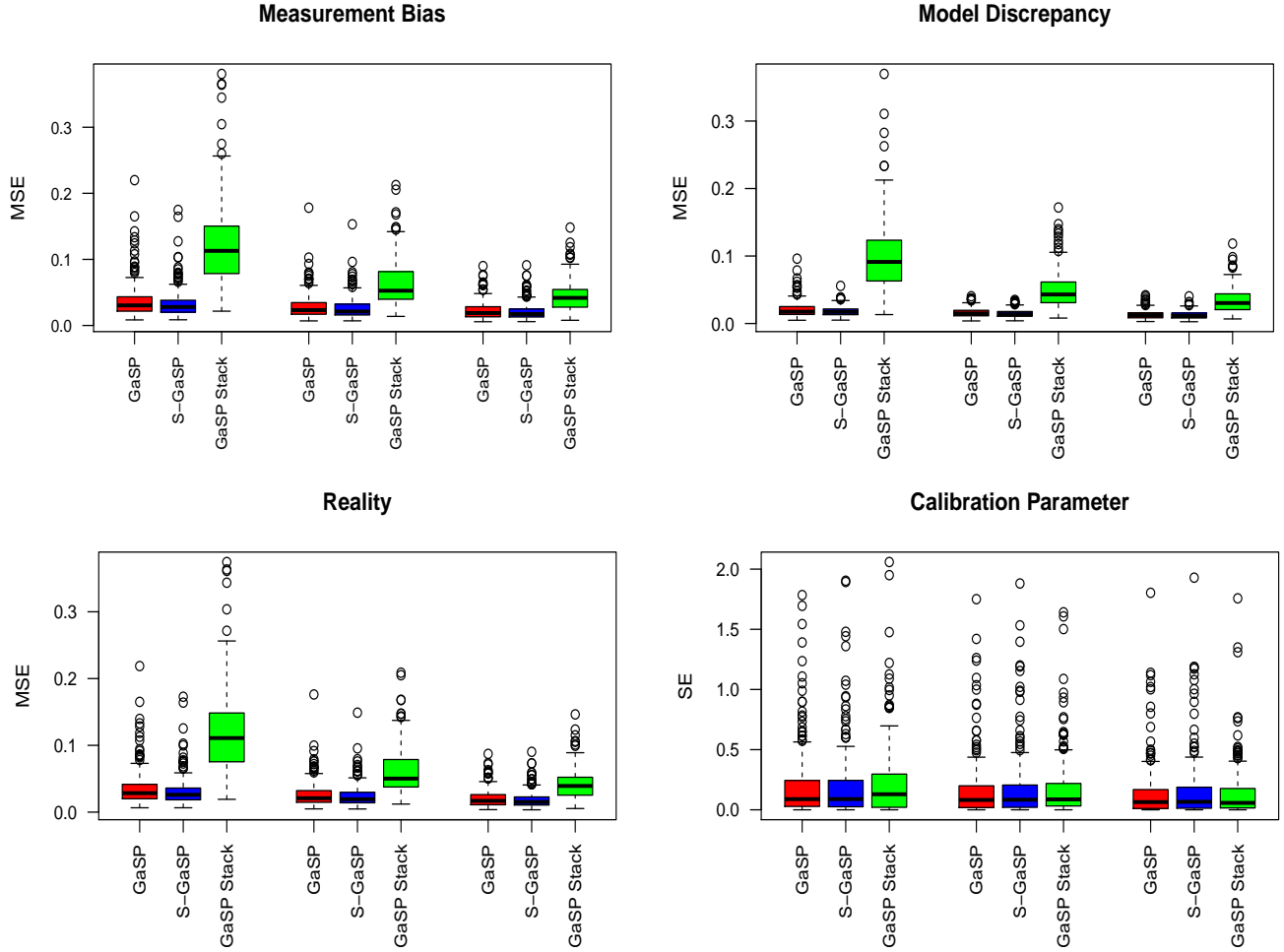


Figure 5: The MSE of estimation of measurement bias discrepancy function, reality and SE of the calibration parameters for Example 3 in each experiment are graphed in the upper left panel, upper right panel, lower left panel and lower right panel, respectively. In each panel, the first three boxes, the middle three boxes and the right three boxes are the results when  $k = 5$ ,  $k = 10$  and  $k = 15$ , respectively. The MSE of GaSP calibration, S-GaSP calibration based on the full data and the GaSP calibration based on the aggregated data are colored as the red, blue and green.

discrepancy function based on multiple sources of data under certain tolerance bound. When the underlying discrepancy function is sampled from a GaSP, typically the uncertainty in estimating the calibration parameter(s) and discrepancy function won't decrease to zero, even if one has infinite number of sources and data and infinite number of observations in each source in a fixed domain. The S-GaSP calibration model also performs relatively well, even if the true discrepancy function is sampled from a GaSP in this example.

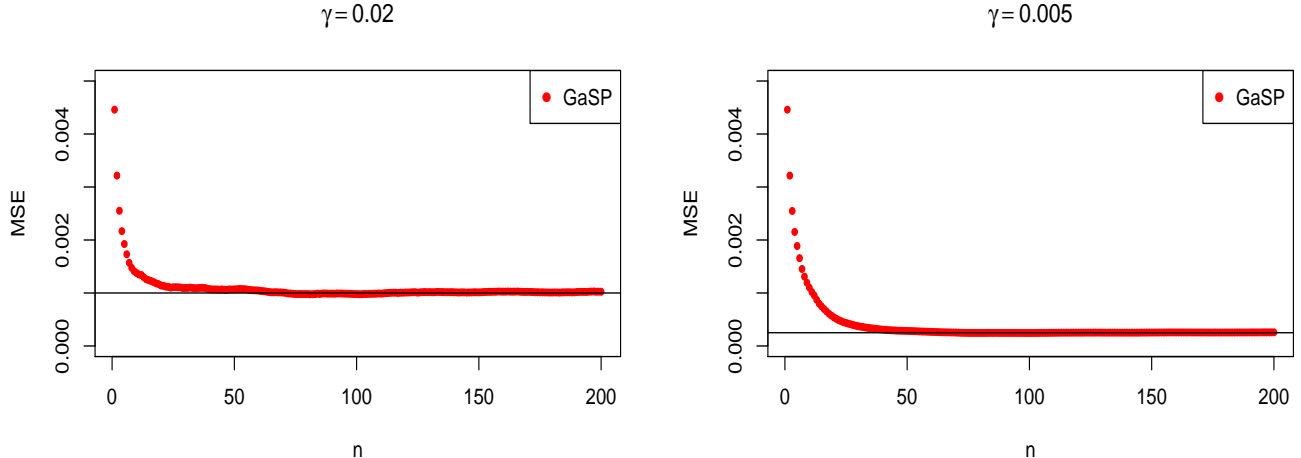


Figure 6: The MSEs of the maximum likelihood estimator of the calibration parameter in Example 3 at different  $n$  when  $k \rightarrow \infty$  with  $\gamma = 0.02$  and  $\gamma = 0.005$  are graphed in the left panel and right panel, respectively. The black lines are 0.001 and 0.00025 in the left panel and right panel.

## 5.2 Geophysical model calibration by InSAR interferograms

In this section, we study the performance of the aforementioned approaches in calibrating the geophysical model of Kīlauea Volcano. Ground deformation velocities computed from interferograms captured by the COSMO-SkyMed satellite spanning different time periods between late 2011 and mid-2012 are shown in Figure 7 (the rate of ground deformation is assumed constant over the complete time range). We first compare the GaSP calibration model in (2) and the S-GaSP calibration model in (26) based on the ground displacement in 400 aligned pixels uniformly sampled from the interferograms. The parameters of the GaSP calibration model and S-GaSP calibration model are given in Table 2. 50,000 posterior samples are drawn with the first 10,000 posterior samples used as the burn-in samples in both models. The posterior samples in every 10th step are used for the analysis to reduce storage space and autocorrelation in the Markov Chain.

Figure 8 graphs the posterior samples of the calibration parameters listed in Table 2 in the GaSP and S-GaSP calibrations. When the discrepancy function is modeled by GaSP, estimates of the chamber depth ( $\theta_3$ ) and magma storage rate ( $\theta_4$ ) are both larger than those of the S-GaSP calibration. This phenomenon was also found in [20], which used only two interferograms for calibration. Here we use five interferograms and model the measurement errors explicitly in the calibration models. Consequently, the posterior samples of the GaSP and S-GaSP calibrations get closer than the results using two interferograms without modeling the measurement bias functions.

The mean squared errors of the predictions on the full interferograms based on 400 uniformly sampled pixels given in Table 3. The mean parameters  $\mu$  are treated as a part of the geophysical model for making predictions. The S-GaSP is designed to have the calibrated geophysical model explain more variability in the observations, and consequently the S-GaSP-calibrated geophysical model is more accurate in predicting the reality (at points not used for calibration) than the one in the GaSP model, shown in the first two rows in Table 3. Furthermore, both the GaSP and S-GaSP models predict the interferograms equally well using the combined calibrated geophysical

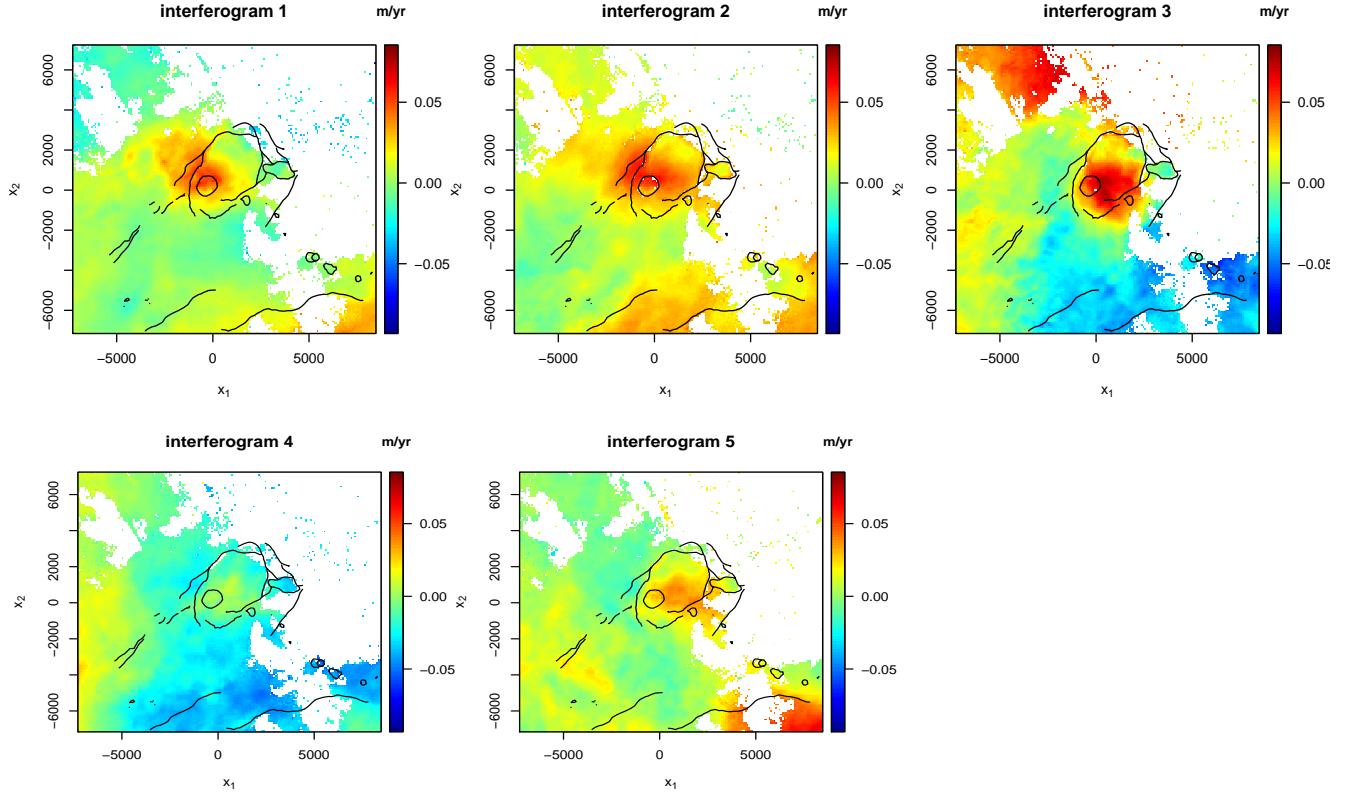


Figure 7: Five COSMO-SkyMed satellite interferograms spanning the following time periods: 1) 17 Oct 2011 - 04 May 2012; 2) 21 Oct 2011 - 16 May 2012; 3) 20 Oct 2011 to 15 May 2012; 4) 28 Oct 2011 to 11 May 2012; 5) 12 Oct 2011 - 07 May 2012. Interferograms 1 and 2 share an ascending-mode look angle, while the rest are descending-mode; as a result, there is an apparent east-west shift in the location of maximum displacement between these groups of images (caused by the oblique angle of the satellite viewing geometry). Horizontal position is in meters relative to an arbitrary point in Kilauea Caldera; vertical scale is m/yr. The black curves show cliffs and other important topographic features at Kilauea (see Figure 1).

model and discrepancy function, shown in the last two rows in Table 3.

Estimated measurement bias and model discrepancy for GaSP and S-GaSP calibrations are shown in Figures 9 and 10, respectively. The estimated model discrepancy in the GaSP calibration suggests that the calibrated geophysical model may underestimate the ground displacement in the southeast region. However, this is very likely to be caused by the atmospheric artifact appearing in the first, second and fifth panel in Figure 8. In comparison, the atmospheric artifact seems to be properly explained as measurement bias in the S-GaSP calibration shown in Figure 10, and the estimated model discrepancy in the S-GaSP calibration is close to zero at all locations.

The calibrated geophysical models by the GaSP calibration and S-GaSP calibration, as well as the trace plots of all the parameters, are shown in the supplementary material. In summary, as these five interferograms may all contain very large measurement bias, the S-GaSP calibration does not detect much discrepancy between the geophysical model and reality during this period of time.

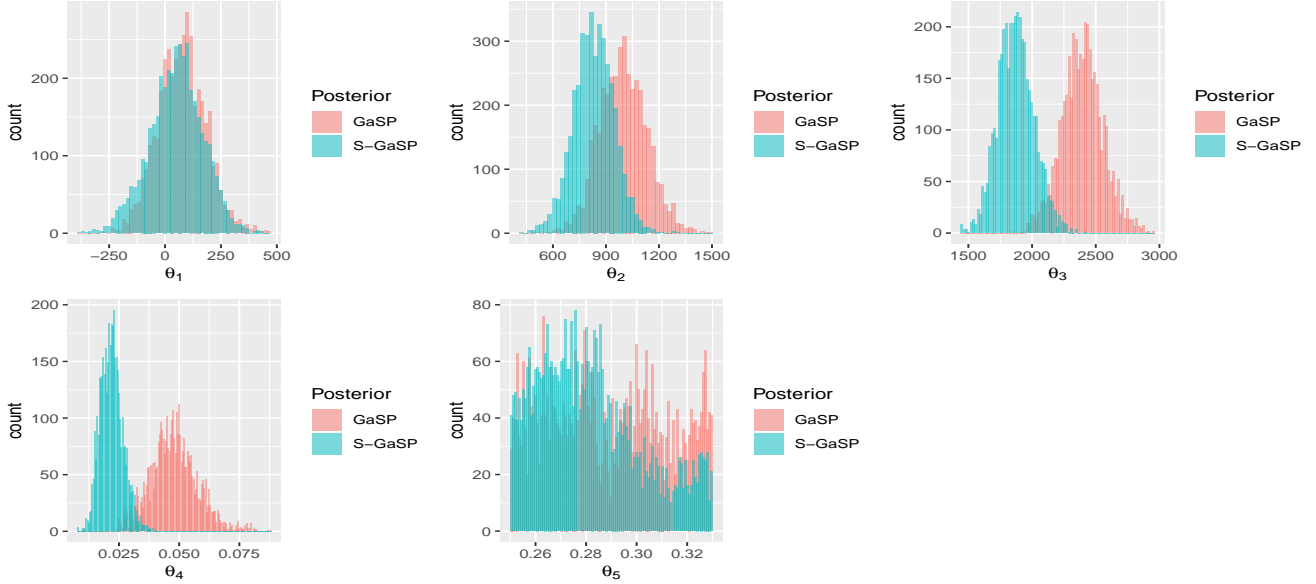


Figure 8: The posterior samples of the calibration parameters in the GaSP and S-GaSP calibrations.

Table 3: Predictive mean squared errors (MSE) in the prediction of the full interferograms by the GaSP and S-GaSP models based on 400 uniformly sampled pixels in each interferogram.  $MSE_{fM}$  is the MSE using the calibrated geophysical model for prediction and  $MSE_{fM+\delta}$  is the MSE using the combined calibrated geophysical model and discrepancy function for prediction.

$MSE_{fM}$	image 1	image 2	image 3	image 4	image 5	mean
GaSP	$1.30 \times 10^{-4}$	$1.71 \times 10^{-4}$	$7.84 \times 10^{-4}$	$4.46 \times 10^{-4}$	$2.04 \times 10^{-4}$	$3.47 \times 10^{-4}$
S-GaSP	<b><math>1.21 \times 10^{-4}</math></b>	<b><math>1.38 \times 10^{-4}</math></b>	<b><math>7.69 \times 10^{-4}</math></b>	<b><math>3.49 \times 10^{-4}</math></b>	<b><math>1.64 \times 10^{-4}</math></b>	<b><math>3.08 \times 10^{-4}</math></b>
$MSE_{fM+\delta}$	image 1	image 2	image 3	image 4	image 5	mean
GaSP	<b><math>1.15 \times 10^{-5}</math></b>	<b><math>1.14 \times 10^{-5}</math></b>	$2.64 \times 10^{-5}$	$1.36 \times 10^{-5}$	<b><math>1.20 \times 10^{-5}</math></b>	$1.50 \times 10^{-5}$
S-GaSP	$1.26 \times 10^{-5}$	$1.23 \times 10^{-5}$	<b><math>2.58 \times 10^{-5}</math></b>	<b><math>1.12 \times 10^{-5}</math></b>	$1.27 \times 10^{-5}$	<b><math>1.49 \times 10^{-5}</math></b>

Next, we compare parameter estimates obtained using individual images to those obtained using image stacks. Each of our five interferograms was captured at one of two different look two angles. We construct two stacks – one for each set of images recorded at each look vector. We compare uniform sampling with the quadtree approach discussed in 4.1. The posterior samples of the GaSP calibration and S-GaSP calibration using stack images are shown in Figure 11. The posterior calibration parameters of all methods using the stack images seem to be close to the posterior mean of the calibration parameters in the S-GaSP calibration using the full data, plotted as the blue dotted lines in each panel. After averaging different images, the stack image has less measurement bias and noise on average. Consequently, the overall range of the ground deformation also gets smaller. As the geophysical model with a comparatively shallow magma chamber and smaller storage rate leads to smaller overall change of the ground deformation, it is not surprising to find that all methods using the stack image agree with the results by the S-GaSP calibration based on the individual images.

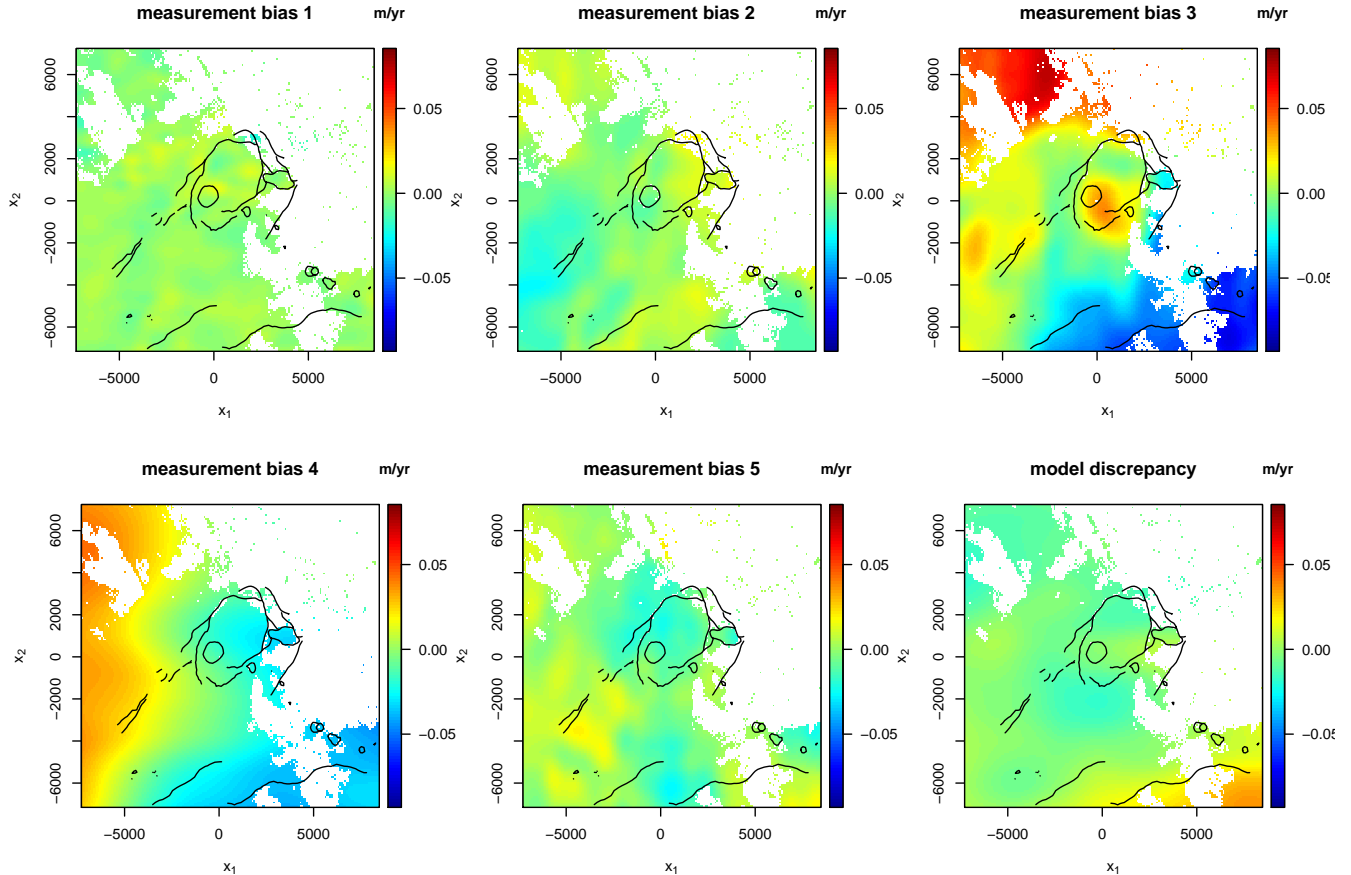


Figure 9: Estimated measurement bias of five interferograms and model discrepancy in the GaSP calibration.

Although image stacks are useful to reduce the measurement bias and noise contained in the observations, one usually loses some information in estimating the measurement bias and discrepancy function using aggregated data, discussed in Section 5.1. Among all approaches, the S-GaSP calibration based on the full data seems to be both robust in estimating the calibration parameters in the presence of the measurement bias and model discrepancy, and accurate in separating measurement bias and model discrepancy from the observations.

Finally, we can compare our results with previous work at the volcano. Two of the interferograms used in this study (the second and third interferograms shown in Figure 7) were also used for calibrating the same geophysical model as part of a broader geophysical study [3], but that work did not consider spatially-correlated noise in the data or a discrepancy function, nor did it utilize more than two interferograms. The same two interferograms were used in [20] for calibration with a discrepancy function, but the measurement bias in the interferograms was overlooked. Of all the images, the ones used in the previous studies show the largest apparent volcanic ground displacement, and as a result the reservoir volume change rate ( $\theta_4$ ) we estimate here in the S-GaSP calibration using all five images is smaller than in those studies ( $0.02 \text{ m}^3/\text{s}$  vs.  $0.04\text{--}0.05 \text{ m}^3/\text{s}$ , respectively). Because our results utilize all data rather than a selection, they may be considered more robust, since a larger number of interferograms would be useful for better resolving signal

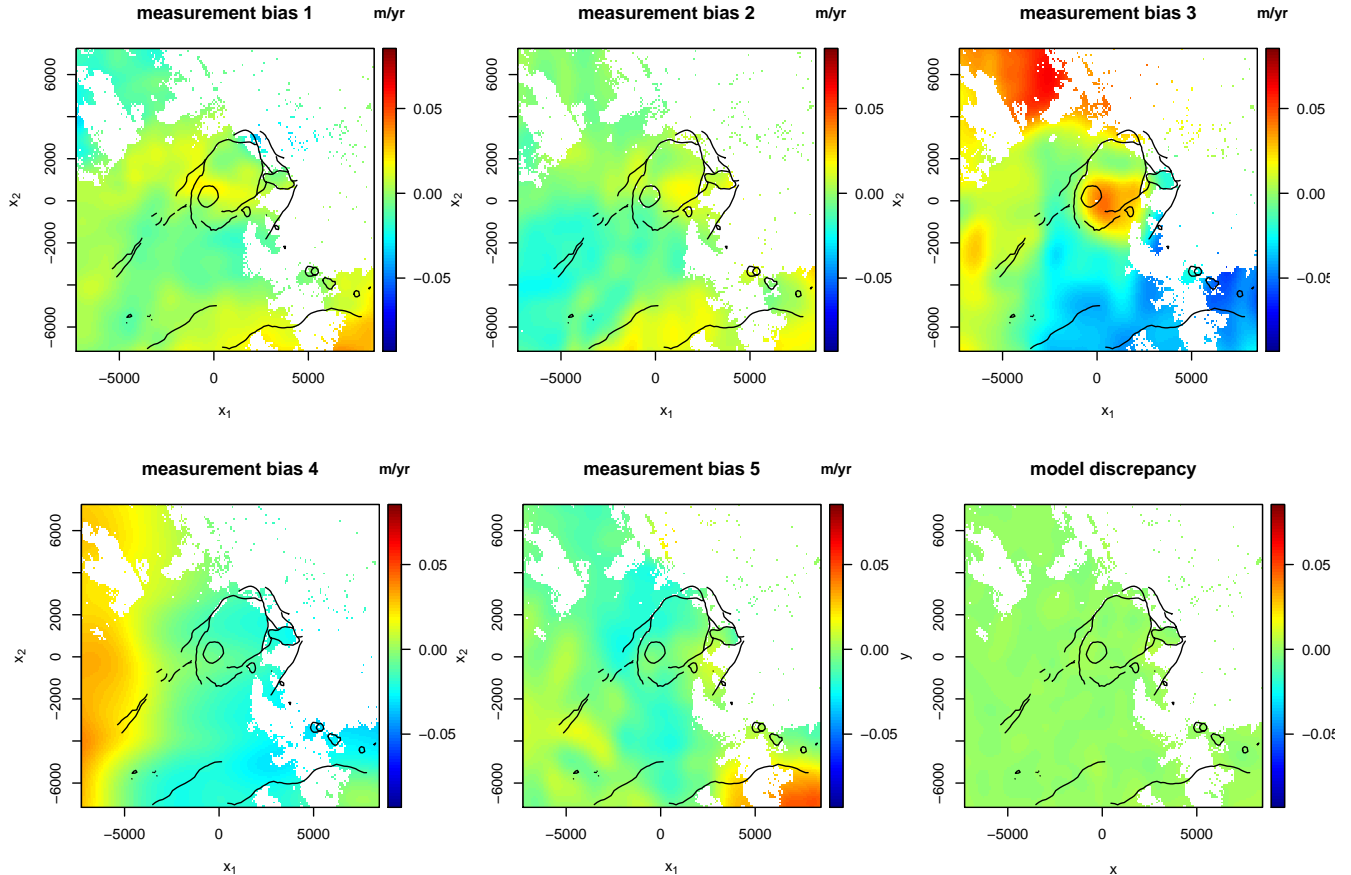


Figure 10: Estimated measurement bias of five interferograms and model discrepancy in the S-GaSP calibration.

from noise. Based on these results we expect that more interferograms should yield a more stable model and accurate model parameter inferences.

Estimated reservoir position depends on the spatial pattern of displacements but not the rate. We estimate a reservoir location  $\sim 500$  m east and  $\sim 800$  m north of the reference position (SE rim of Halema‘uma‘u Crater), at 1.9 km depth. Many previous studies have examined reservoir location using a variety of data sets over many years. Despite the relatively low signal-to-noise ratio in the data, our estimated depth is consistent with these studies (e.g., [5, 42]). The horizontal position of our most likely reservoir centroid is several hundred meters north of the most commonly-accepted location near the east rim of Halema‘uma‘u Crater [5, 42], but is closer than the position estimated previously in [3] and [20] using two interferograms without modeling the measurement bias; this confirms the importance of addressing the uncertainty in the measurement bias in multiple interferograms. In the future we hope to combine not only multiple measurements of a single type, but also multiple types of data (for instance, GPS or tilt). We also note that in this study the geophysical model and atmospheric noise together are able to explain almost all of the observed signal (model discrepancy is close to zero in the S-GaSP calibration), but future studies utilizing data sets with larger geophysical signals may invoke an important component of model discrepancy.

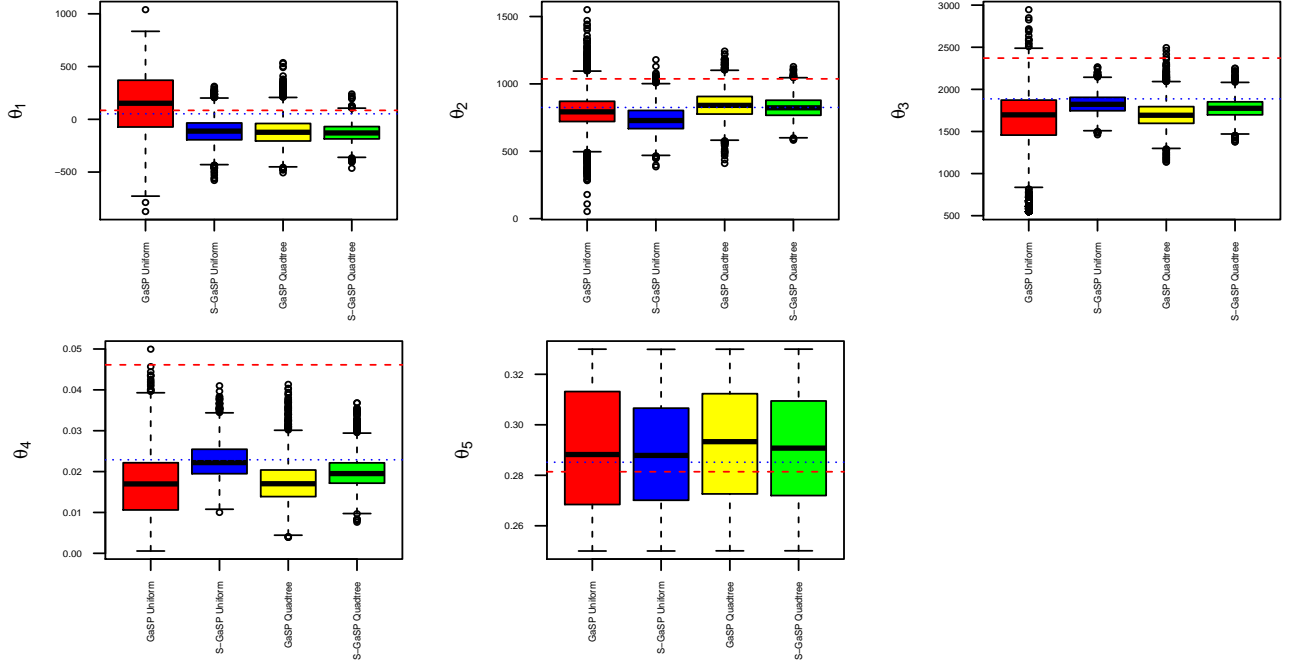


Figure 11: The posterior samples of calibration parameters by image stacking in the GaSP calibration and S-GaSP calibration based on Uniform design and the Quadtree design of the stack images. The red dashed lines and the blue dotted lines are the posterior mean in the GaSP calibration and S-GaSP calibration based on the five individual images, respectively.

## 6 Concluding remarks

We have introduced a statistical framework to estimate measurement bias, model discrepancy, and calibration parameters using multiple sources of data. There are several possible future extensions. First of all, the computation based on the full data scales linearly with the number of data sources when the inputs are aligned. When the inputs are misaligned, it will be helpful to design an exact or approximate algorithm for computational purposes. Second, the quadtree-processed images are used widely in downsampling satellite interferograms. A theoretical study on how to model the quadtree images that properly takes into account the size of the boxes and the measurement bias will be very useful. It is also interesting to study whether the quadtree-processed images improve the accuracy in calibration and prediction compared to some other alternate designs. Lastly, other observations such as the gas emission data and GPS data can also be helpful to calibrate and verify the geophysical model of Kīlauea Volcano.

## Appendix: Proofs

*Proof of lemma 1.* Marginalizing out  $\delta_l$ , based on the laws of the total expectation and total variance, the marginal distribution of  $\mathbf{y}_l^F$  is a multivariate normal distribution with the mean

$$\begin{aligned}\mathbb{E}[\mathbf{y}_l^F \mid \boldsymbol{\delta}, \boldsymbol{\theta}, \sigma_l^2, \mathbf{R}_l, \mu_l, \sigma_{0l}^2] &= \mathbb{E}[\mathbb{E}[\mathbf{y}_l^F \mid \boldsymbol{\delta}, \boldsymbol{\theta}, \sigma_l^2, \mathbf{R}_l, \mu_l, \sigma_{0l}^2, \boldsymbol{\delta}_l]] \\ &= \mathbf{f}_\theta^M + \mu_l \mathbf{1}_n + \boldsymbol{\delta},\end{aligned}$$

and the covariance matrix

$$\begin{aligned}\mathbb{V}[\mathbf{y}_l^F \mid \boldsymbol{\delta}, \boldsymbol{\theta}, \sigma_l^2, \mathbf{R}_l, \mu_l, \sigma_{0l}^2] &= \mathbb{V}[\mathbb{E}[\mathbf{y}_l^F \mid \boldsymbol{\delta}, \boldsymbol{\theta}, \sigma_l^2, \mathbf{R}_l, \mu_l, \sigma_{0l}^2, \boldsymbol{\delta}_l]] + \mathbb{E}[\mathbb{V}[\mathbf{y}_l^F \mid \boldsymbol{\delta}, \boldsymbol{\theta}, \sigma_l^2, \mathbf{R}_l, \mu_l, \sigma_{0l}^2, \boldsymbol{\delta}_l]] \\ &= \mathbb{V}[\mathbf{f}_\theta^M + \mu_l \mathbf{1}_n + \boldsymbol{\delta} + \boldsymbol{\delta}_l \mid \boldsymbol{\delta}, \boldsymbol{\theta}, \sigma_l^2, \mathbf{R}_l, \mu_l, \sigma_{0l}^2] + \sigma_{0l}^2 \mathbf{I}_n \\ &= \sigma_l^2 \mathbf{R}_l + \sigma_{0l}^2 \mathbf{I}_n,\end{aligned}$$

from which (5) follows.

After marginalizing out  $\{\boldsymbol{\delta}_l\}_{l=1}^k$ , the posterior distribution of  $\boldsymbol{\delta}$  follows a multivariate normal distribution with the mean and covariance matrix given in (6), from which the proof is complete.  $\square$

*Proof of Lemma 2.* After marginalizing out  $\delta_l$ ,  $l = 1, \dots, k$ , one has

$$(\mathbf{Y}_v^F \mid \{\sigma_l^2, \mathbf{R}_l, \sigma_{0l}^2, \mu_l\}_{l=1}^k, \boldsymbol{\delta}, \boldsymbol{\theta}, \tau^2, \mathbf{R}) \sim \text{MN}(\mathbf{1}_k \otimes \mathbf{f}_\theta^M + \boldsymbol{\mu} \otimes \mathbf{1}_n + \mathbf{1}_k \otimes \boldsymbol{\delta}, \boldsymbol{\Lambda}), \quad (31)$$

where  $\boldsymbol{\Lambda}$  is a block diagonal matrix with the  $l$ th diagonal block being  $\tilde{\boldsymbol{\Sigma}}_l$ ,  $l = 1, \dots, k$ .

Note  $(\boldsymbol{\delta} \mid \tau^2, \mathbf{R}) \sim \text{MN}(\mathbf{0}, \tau^2 \mathbf{R})$ . Further marginalizing out  $\boldsymbol{\delta}$ , the marginal distribution of  $(\mathbf{Y}^F \mid \{\sigma_l^2, \mathbf{R}_l, \sigma_{0l}^2, \mu_l\}_{l=1}^k, \boldsymbol{\theta}, \tau^2, \mathbf{R})$  follows a multivariate normal distribution, with the mean

$$\mathbb{E}[\mathbf{Y}_v^F \mid \{\sigma_l^2, \mathbf{R}_l, \sigma_{0l}^2, \mu_l\}_{l=1}^k, \boldsymbol{\theta}, \tau^2, \mathbf{R}] = \mathbb{E}[\mathbb{E}[\mathbf{Y}_v^F \mid \{\sigma_l^2, \mathbf{R}_l, \sigma_{0l}^2, \mu_l\}_{l=1}^k, \boldsymbol{\delta}, \boldsymbol{\theta}, \tau^2, \mathbf{R}]] = \mathbf{1}_k \otimes \mathbf{f}_\theta^M.$$

and the posterior variance

$$\begin{aligned}\mathbb{V}[\mathbf{Y}_v^F \mid \{\sigma_l^2, \mathbf{R}_l, \sigma_{0l}^2, \mu_l\}_{l=1}^k, \boldsymbol{\theta}, \tau^2, \mathbf{R}] &= \mathbb{V}[\mathbb{E}[\mathbf{Y}_v^F \mid \{y_l^F, \tilde{\boldsymbol{\Sigma}}_l, \mu_l\}_{l=1}^k, \boldsymbol{\delta}, \boldsymbol{\theta}, \tau^2, \mathbf{R}]] + \mathbb{E}[\mathbb{V}[\mathbf{Y}_v^F \mid \{y_l^F, \tilde{\boldsymbol{\Sigma}}_l, \mu_l\}_{l=1}^k, \boldsymbol{\delta}, \boldsymbol{\theta}, \tau^2, \mathbf{R}]] \\ &= \mathbb{V}[\mathbf{1}_k \otimes \mathbf{f}_\theta^M + \boldsymbol{\mu} \otimes \mathbf{1}_n + \mathbf{1}_k \otimes \boldsymbol{\delta} \mid \{\sigma_l^2, \mathbf{R}_l, \sigma_{0l}^2, \mu_l\}_{l=1}^k, \boldsymbol{\theta}, \tau^2, \mathbf{R}] + \boldsymbol{\Lambda} \\ &= \mathbf{1}_k \mathbf{1}_k^T \otimes (\tau^2 \mathbf{R}) + \boldsymbol{\Lambda},\end{aligned}$$

from which (7) follows. Note that the density of  $(\mathbf{Y}_v^F, \boldsymbol{\delta})$  follows

$$\begin{aligned}p(\mathbf{Y}_v^F, \boldsymbol{\delta} \mid \{\sigma_l^2, \mathbf{R}_l, \sigma_{0l}^2, \mu_l\}_{l=1}^k, \boldsymbol{\theta}, \tau^2, \mathbf{R}) &= \prod_{l=1}^k \left\{ (2\pi)^{-\frac{n}{2}} |\tilde{\boldsymbol{\Sigma}}_l|^{-\frac{1}{2}} \exp\left(-\frac{(\tilde{\mathbf{y}}_l - \boldsymbol{\delta})^T \tilde{\boldsymbol{\Sigma}}_l^{-1} (\tilde{\mathbf{y}}_l - \boldsymbol{\delta})}{2}\right) \right\} (2\pi\tau^2)^{-\frac{n}{2}} |\mathbf{R}|^{-\frac{1}{2}} \exp\left(-\frac{\boldsymbol{\delta}^T \mathbf{R}^{-1} \boldsymbol{\delta}}{2\tau^2}\right).\end{aligned}$$

Direct marginalizing out  $\boldsymbol{\delta}$  from the above equation yields the density of  $(\mathbf{Y}_v^F \mid \{\sigma_l^2, \mathbf{R}_l, \sigma_{0l}^2, \mu_l\}_{l=1}^k, \boldsymbol{\theta}, \tau^2, \mathbf{R})$ .  $\square$

*Proof of Theorem 1.* We only verify the third claim and the previous two claims can be verified similarly. For the third claim, the mean follows

$$\begin{aligned}\mathbb{E}[\mathbf{y}_l^F(\mathbf{x}^*) \mid \boldsymbol{\delta}, \{\mathbf{y}_l^F, \sigma_l^2, K_l(\cdot, \cdot), \sigma_{0l}^2, \mu_l\}_{l=1}^k, \boldsymbol{\theta}, \tau^2, K(\cdot, \cdot)] &= \mathbb{E}[\boldsymbol{\delta}(\mathbf{x}^*) + \delta_l(\mathbf{x}^*) + f^M(\mathbf{x}^*, \boldsymbol{\theta}) + \mu_l \mid \boldsymbol{\delta}, \{\mathbf{y}_l^F, \sigma_l^2, K_l(\cdot, \cdot), \sigma_{0l}^2, \mu_l\}_{l=1}^k, \boldsymbol{\theta}, \tau^2, K(\cdot, \cdot)] \\ &= \mathbf{r}(\mathbf{x}^*)^T \mathbf{R}^{-1} \boldsymbol{\delta} + \sigma_l^2 \mathbf{r}_l(\mathbf{x}^*) \tilde{\boldsymbol{\Sigma}}_l^{-1} (\mathbf{y}_l^F - \mathbf{f}_\theta^M - \mu_l \mathbf{1}_n - \boldsymbol{\delta}) + f^M(\mathbf{x}^*, \boldsymbol{\theta}) + \mu_l = \hat{\boldsymbol{\delta}}(\mathbf{x}^*) + \hat{\delta}_l(\mathbf{x}^*) + f^M(\mathbf{x}^*, \boldsymbol{\theta}) + \mu_l,\end{aligned}$$

and the variance is

$$\begin{aligned}
& \mathbb{V} [\mathbf{y}_l^F(\mathbf{x}^*) \mid \boldsymbol{\delta}, \{\mathbf{y}_l^F, \sigma_l^2, K_l(\cdot, \cdot), \sigma_{0l}^2, \mu_l\}_{l=1}^k, \boldsymbol{\theta}, \tau^2, K(\cdot, \cdot)] \\
&= \mathbb{V} [\mathbb{E} [\mathbf{y}_l^F(\mathbf{x}^*) \mid \boldsymbol{\delta}, \{\mathbf{y}_l^F, \sigma_l^2, K_l(\cdot, \cdot), \sigma_{0l}^2, \mu_l\}_{l=1}^k, \boldsymbol{\theta}, \tau^2, K(\cdot, \cdot), \delta(\mathbf{x}^*), \delta_l(\mathbf{x}^*)]] + \sigma_{l0}^2 \\
&= \mathbb{V} [\delta(\mathbf{x}^*) + \delta_l(\mathbf{x}^*) + f^M(\mathbf{x}^*, \boldsymbol{\theta}) + \mu_l \mid \boldsymbol{\delta}, \mathbf{y}_l^F, \sigma_l^2, K_l(\cdot, \cdot), \sigma_{0l}^2, \mu_l, \boldsymbol{\theta}, \tau^2, K(\cdot, \cdot)] + \sigma_{l0}^2 \\
&= \tau^2 \hat{K}^{**} + \sigma_l^2 \hat{K}_l^{**} + \sigma_{l0}^2.
\end{aligned}$$

The claim soon follows by noticing the predictive distribution is a multivariate normal distribution.  $\square$

*Proof of Lemma 5.* First by Lemma 3, as the sampling model is (8), the MLE of the calibration parameter is the same as using the full data or the aggregated data  $\bar{\mathbf{y}}^F$ . Based on the limiting distribution of the aggregated data in Theorem 2, when  $k \rightarrow \infty$ , the MLE of the calibration parameter is  $\hat{\theta}_{MLE} = (\mathbf{1}_n^T \mathbf{R}^{-1} \mathbf{1}_n)^{-1} \mathbf{1}_n^T \mathbf{R}^{-1} \bar{\mathbf{y}}^F$  with the sampling distribution

$$\hat{\theta}_{MLE} \sim \text{N}(\theta, \tau^2 (\mathbf{1}_n^T \mathbf{R}^{-1} \mathbf{1}_n)^{-1}).$$

Denote  $\rho_n = \exp(-\frac{1}{n\gamma})$ . The inverse correlation matrix can be computed explicitly [21]

$$\mathbf{R}^{-1} = \frac{1}{1 - \rho_n^2} \begin{pmatrix} 1 & -\rho_n & 0 & 0 & \dots & 0 \\ -\rho_n & 1 + \rho_n^2 & -\rho_n & 0 & \dots & 0 \\ 0 & -\rho_n & 1 + \rho_n^2 & -\rho_n & \dots & 0 \\ \vdots & \vdots & \vdots & \ddots & \vdots & \vdots \\ 0 & 0 & \dots & -\rho_n & 1 + \rho_n^2 & -\rho_n \\ 0 & 0 & \dots & 0 & -\rho_n & 1 \end{pmatrix}.$$

When  $n \rightarrow \infty$ , the variance of the sampling distribution of  $\hat{\theta}_{MLE}$  is

$$\begin{aligned}
\mathbb{V}[\theta_{MLE}] &= \lim_{n \rightarrow \infty} \tau^2 (\mathbf{1}_n^T \mathbf{R}^{-1} \mathbf{1}_n)^{-1} \\
&= \lim_{n \rightarrow \infty} \tau^2 \frac{1 - \rho_n^2}{(1 - \rho_n)(n - (n - 2)\rho_n)} \\
&= \lim_{n \rightarrow \infty} \tau^2 \frac{1 - \exp(-\frac{2}{n\gamma})}{(1 - \exp(-\frac{1}{n\gamma}))(n - (n - 2)\exp(-\frac{1}{n\gamma}))} \\
&= \frac{2\tau^2\gamma}{2\gamma + 1},
\end{aligned}$$

where the last line follows from the Taylor expansion. This completes the proof.  $\square$

## References

- [1] Amelung, F., Jonsson, S., Zebker, H., and Segall, P. (2000). Widespread uplift and 'trapdoor' faulting on Galapagos volcanoes observed with radar interferometry. *Nature*, 407(6807):993–996.
- [2] Anderson, K. and Segall, P. (2011). Physics-based models of ground deformation and extrusion rate at effusively erupting volcanoes. *Journal of Geophysical Research: Solid Earth*, 116(B7).

- [3] Anderson, K. R. and Poland, M. P. (2016). Bayesian estimation of magma supply, storage, and eruption rates using a multiphysical volcano model: Kīlauea volcano, 2000–2012. *Earth and Planetary Science Letters*, 447:161–171.
- [4] Anderson, K. R. and Poland, M. P. (2017). Abundant carbon in the mantle beneath hawaii/i. *Nature Geoscience*, 10(9):704–708.
- [5] Anderson, K. R., Poland, M. P., Johnson, J. H., and Miklius, A. (2015). Episodic deflation-inflation events at Kīlauea Volcano and implications for the shallow magma system. In Carey, R. J., Poland, M., Cayol, V., and Weis, D., editors, *Hawaiian volcanoes, from source to surface*, chapter 11, pages 229–250. AGU Geophysical Monograph 208.
- [6] Arendt, P. D., Apley, D. W., and Chen, W. (2012). Quantification of model uncertainty: Calibration, model discrepancy, and identifiability. *Journal of Mechanical Design*, 134(10):100908.
- [7] Baker, S. and Amelung, F. (2012). Top-down inflation and deflation at the summit of Kīlauea Volcano, Hawaii observed with InSAR. *Journal of Geophysical Research B: Solid Earth*, 117(12):1–14.
- [8] Bayarri, M. J., Berger, J. O., Paulo, R., Sacks, J., Cafeo, J. A., Cavendish, J., Lin, C.-H., and Tu, J. (2007). A framework for validation of computer models. *Technometrics*, 49(2):138–154.
- [9] Biggs, J. and Pritchard, M. E. (2017). Global Volcano Monitoring: What Does It Mean When Volcanoes Deform? *Elements*, 13(1):17–22.
- [10] Bürgmann, R., Rosen, P. A., and Fielding, E. J. (2000). Synthetic Aperture Radar Interferometry to Measure Earth’s Surface Topography and Its Deformation. *Annual Review of Earth and Planetary Sciences*, 28(1):169–209.
- [11] Chen, C. W. and Zebker, H. A. (2001). Two-dimensional phase unwrapping with use of statistical models for cost functions in nonlinear optimization. *Journal of the Optical Society of America A*, 18(2):338.
- [12] Chen, J., Zebker, H. a., Segall, P., and Miklius, A. (2014). The 2010 slow slip event and secular motion at Kīlauea, Hawai‘i inferred from TerraSAR-X InSAR data. *Journal of Geophysical Research: Solid Earth*, pages n/a–n/a.
- [13] Foster, J., Brooks, B., Cherubini, T., Shacat, C., Businger, S., and Werner, C. (2006). Mitigating atmospheric noise for insar using a high resolution weather model. *Geophysical Research Letters*, 33(16).
- [14] Frenklach, M., Packard, A., Garcia-Donato, G., Paulo, R., and Sacks, J. (2016). Comparison of statistical and deterministic frameworks of uncertainty quantification. *SIAM/ASA Journal on Uncertainty Quantification*, 4(1):875–901.
- [15] Gelfand, A. E., Schmidt, A. M., Banerjee, S., and Sirmans, C. (2004). Nonstationary multivariate process modeling through spatially varying coregionalization. *Test*, 13(2):263–312.

- [16] Gong, W., Lu, Z., and Meyer, F. (2016). Uncertainties in estimating magma source parameters from InSAR observation. In Riley, K., Webley, P., and Thompson, M., editors, *Natural Hazard Uncertainty Assessment: Modeling and Decision Support, Geophysical Monograph 223*, chapter 7, pages 89–104. John Wiley & Sons, Inc.
- [17] Gu, M. (2018a). Jointly robust prior for Gaussian stochastic process in emulation, calibration and variable selection. *Bayesian Analysis, In Press. arXiv preprint arXiv:1804.09329*.
- [18] Gu, M. (2018b). *RobustCalibration: Robust Calibration of Imperfect Mathematical Models*. R package version 0.5.2.
- [19] Gu, M. and Shen, W. (2018). Generalized probabilistic principal component analysis of correlated data. *arXiv preprint arXiv:1808.10868*.
- [20] Gu, M. and Wang, L. (2017). Scaled Gaussian stochastic process for computer model calibration and prediction. *SIAM/ASA Journal on Uncertainty Quantification, In Press. arXiv preprint arXiv:1707.08215*.
- [21] Gu, M., Wang, X., and Berger, J. O. (2018a). Robust Gaussian stochastic process emulation. *Annals of Statistics*, 46(6A):3038–3066.
- [22] Gu, M., Xie, F., and Wang, L. (2018b). A theoretical framework of the scaled Gaussian stochastic process in prediction and calibration. *arXiv preprint arXiv:1807.03829*.
- [23] Higdon, D., Gattiker, J., Williams, B., and Rightley, M. (2008). Computer model calibration using high-dimensional output. *Journal of the American Statistical Association*, 103(482):570–583.
- [24] Hodges, J. S. and Reich, B. J. (2010). Adding spatially-correlated errors can mess up the fixed effect you love. *The American Statistician*, 64(4):325–334.
- [25] Hooper, A., Bekaert, D., Spaans, K., and Arikan, M. (2012). Recent advances in SAR interferometry time series analysis for measuring crustal deformation. *Tectonophysics*, 514–517:1–13.
- [26] Hooper, A., Segall, P., and Zebker, H. (2007). Persistent Scatterer InSAR for Crustal Deformation Analysis, with Application to Volcan Alcedo, Galapagos. *Journal of Geophysical Research*, 112:1–19.
- [27] Jonsson, S., Zebker, H., Segall, P., and Amelung, F. (2002). Fault Slip Distribution of the 1999 Mw 7.1 Hector Mine, California, Earthquake, Estimated from Satellite Radar and GPS Measurements. *Bulletin of the Seismological Society of America*, 92(4):1377–1389.
- [28] Kennedy, M. C. and O’Hagan, A. (2001). Bayesian calibration of computer models. *Journal of the Royal Statistical Society: Series B (Statistical Methodology)*, 63(3):425–464.
- [29] Knospe, S. and Jonsson, S. (2010). Covariance estimation for dinsar surface deformation measurements in the presence of anisotropic atmospheric noise. *IEEE Transactions on Geoscience and Remote Sensing*, 48(4):2057–2065.

- [30] Lim, Y. B., Sacks, J., Studden, W., and Welch, W. J. (2002). Design and analysis of computer experiments when the output is highly correlated over the input space. *Canadian Journal of Statistics*, 30(1):109–126.
- [31] Lohman, R. B. and Simons, M. (2005). Some thoughts on the use of InSAR data to constrain models of surface deformation: Noise structure and data downsampling. *Geochemistry, Geophysics, Geosystems*, 6(1):n/a–n/a.
- [32] Lu, Z. (2007). InSAR imaging of volcanic deformation over cloud-prone areas - Aleutian islands. *Photogrammetric Engineering and Remote Sensing*, 73(3):245–257.
- [33] Lundgren, P., Poland, M., Miklius, A., Orr, T., Yun, S.-h., Fielding, E., Liu, Z., Tanaka, A., Szeliga, W., Hensley, S., and Owen, S. (2013). Evolution of dike opening during the March 2011 Kamoamoia fissure eruption, Kilauea Volcano, Hawai‘i. *Journal of Geophysical Research: Solid Earth*, 118(3):897–914.
- [34] Massonnet, D., Briole, P., and Arnaud, A. (1995). Deflation of Mount Etna monitored by spaceborne radar interferometry. *Nature*, 375(6532):567–570.
- [35] Massonnet, D., Rossi, M., Carmona, C., Adragna, F., Peltzer, G., Feigl, K., and Rabautte, T. (1993). The displacement field of the Landers earthquake mapped by radar interferometry. *Nature*, 364(6433):138–142.
- [36] Mogi, K. (1958). Relations between the eruptions of various volcanoes and the deformations of the ground surfaces around them. *Bull. Earthquake Res. Inst. University of Tokyo*, 36:99–134.
- [37] Montgomery-Brown, E. K., Sinnott, D. K., Poland, M., Segall, P., Orr, T., Zebker, H., and Miklius, A. (2010). Geodetic evidence for an echelon dike emplacement and concurrent slow slip during the June 2007 intrusion and eruption at Kilauea volcano, Hawaii. *Journal of Geophysical Research*, 115(B7):B07405.
- [38] Montgomery-Brown, E. K., Wicks, C. W., Cervelli, P. F., Langbein, J. O., Svarc, J. L., Shelly, D. R., Hill, D. P., and Lisowski, M. (2015). Renewed inflation of Long Valley Caldera, California (2011 to 2014). *Geophysical Research Letters*, 42(13):5250–5257.
- [39] Nocedal, J. (1980). Updating quasi-newton matrices with limited storage. *Mathematics of computation*, 35(151):773–782.
- [40] Oliver, D. S. and Alfonzo, M. (2018). Calibration of imperfect models to biased observations. *Computational Geosciences*, 22(1):145–161.
- [41] Pinel, V., Poland, M., and Hooper, a. (2014). Volcanology: Lessons learned from Synthetic Aperture Radar imagery. *Journal of Volcanology and Geothermal Research*, 289:81–113.
- [42] Poland, M. P., Miklius, A., and Montgomery-Brown, E. K. (2014). Magma Supply, Storage, and Transport at Shield-Stage Hawaiian Volcanoes. In Poland, M. P., Takahashi, T. J., and Landowski, C. M., editors, *Characteristics of Hawaiian Volcanoes*, chapter 5, pages 179–234. U.S. Geological Survey Professional Paper 1801.

- [43] Pritchard, M., Simons, M., Rosen, P., Hensley, S., and Webb, F. (2002). Co-seismic slip from the 1995 July 30  $M_w = 8.1$  Antofagasta, Chile, earthquake as constrained by InSAR and GPS observations. *Geophysical Journal International*, 150(2):362–376.
- [44] Reich, B. J., Hodges, J. S., and Zadnik, V. (2006). Effects of residual smoothing on the posterior of the fixed effects in disease-mapping models. *Biometrics*, 62(4):1197–1206.
- [45] Santner, T. J., Williams, B. J., and Notz, W. I. (2003). *The design and analysis of computer experiments*. Springer Science & Business Media.
- [46] Simons, M., Fialko, Y., and Rivera, L. (2002). Coseismic deformation from the 1999  $M_w 7.1$  Hector Mine, California, earthquake as inferred from InSAR and GPS observations. *Bulletin of the Seismological Society of America*, 92(4):1390–1402.
- [47] Simons, M. and Rosen, P. A. (2007). Interferometric synthetic aperture radar geodesy. In *Treatise on Geophysics*, volume 3, pages 391–446. Elsevier Press.
- [48] Stein, M. L. (2012). *Interpolation of spatial data: some theory for kriging*. Springer Science & Business Media.
- [49] Sudhaus, H. and Jónsson, S. (2009). Improved source modelling through combined use of InSAR and GPS under consideration of correlated data errors: application to the June 2000 Kleifarvatn earthquake, Iceland. *Geophysical Journal International*, 176(2):389–404.
- [50] Tuo, R. and Wu, C. J. (2015). Efficient calibration for imperfect computer models. *The Annals of Statistics*, 43(6):2331–2352.
- [51] Wang, C., Ding, X., Li, Q., and Jiang, M. (2014). Equation-based InSAR data quadtree downsampling for earthquake slip distribution inversion. *IEEE Geoscience and Remote Sensing Letters*, 11(12):2060–2064.
- [52] Wicks Jr., C. (1998). Migration of Fluids Beneath Yellowstone Caldera Inferred from Satellite Radar Interferometry. *Science*, 282(5388):458–462.
- [53] Wong, R. K., Storlie, C. B., and Lee, T. (2017). A frequentist approach to computer model calibration. *Journal of the Royal Statistical Society: Series B (Statistical Methodology)*, 79:635–648.
- [54] Yang, X.-M. M., Davis, P. M., and Dieterich, J. H. (1988). Deformation from Inflation of a Dipping Finite Prolate Spheroid in an Elastic Half-Space as a Model for Volcanic Stressing. *Journal of Geophysical Research-Solid Earth and Planets*, 93(B5):4249–4257.
- [55] Zebker, H. A., Rosen, P. A., and Hensley, S. (1997). Atmospheric effects in interferometric synthetic aperture radar surface deformation and topographic maps. *Journal of Geophysical Research: Solid Earth*, 102(B4):7547–7563.